
This manuscript is a preprint and will be submitted to **AAPG Bulletin**. This manuscript has not undergone peer-review. Subsequent versions of this manuscript may have different content. If accepted, the final version of this manuscript will be available via the '*Peer-reviewed Publication DOI*' link on the right-hand side of this webpage. Please feel free to contact any of the authors directly or to comment on the manuscript using **hypothes.is** (<https://web.hypothes.is/>). We welcome feedback!

Lithological, petrophysical and seal properties of mass-transport complexes (MTCs), northern Gulf of Mexico

Nan Wu¹, Christopher A-L. Jackson¹, Howard D. Johnson¹, David M. Hodgson²

¹Basins Research Group, Department of Earth Science & Engineering, Imperial College, Prince Consort Road, London, SW7 2BP, UK

²School of Earth and Environment, University of Leeds, Leeds, LS2 9JT, UK

*Email: n.wu16@imperial.ac.uk

Abstract

Mass transport complexes (MTCs) are one of the most sedimentologically and seismically distinctive depositional elements in many deep-water depositional systems. Seismic reflection data provide spectacular images of the structure, size, and distribution of MTCs. However, a dearth of borehole data means that there is limited direct calibration of MTC lithology to their petrophysical response, or knowledge of how they may act as hydrocarbon reservoir seals. In this study, we evaluate the lithological and petrophysical properties, and seismic reflection characteristics of three deeply-buried (>2300 m), Pleistocene MTCs in the northern Gulf of Mexico. Using high-quality 3D seismic reflection and borehole data we show that: (i) MTC lithology is highly variable, comprising a mudstone-rich debrite matrix containing large (4.5 km³) deformed sandstone-rich blocks; (ii) generally, MTCs are acoustically faster and are more resistive than lithologically similar (i.e. mudstone-dominated) slope deposits occurring at a similar burial depth; (iii) MTC velocity and resistivity increase with depth, likely reflecting an overall downward increase in the degree of compaction; (iv) the lowermost 15-30 m of the MTCs, which represent the basal shear zones, are characterised by relatively high P-wave velocity and resistivity values due to shear-induced over-compaction; and (v) large, sandstone-rich blocks within one of the MTCs are under-compacted and thus possibly porous, and could therefore act as potential reservoirs or fluid flow conduits. We conclude that detailed analysis of petrophysical data, in particular velocity and resistivity logs, may allow recognition of MTCs in the absence of high-quality seismic reflection data, including explicit identification of the basal shear zone. Furthermore, the relatively thick basal shear zone, rather than the overlying and substantially thicker MTC itself, may form the primary permeability barrier and thus seal for underlying hydrocarbon accumulations.

1 Introduction

Mass-transport complexes (MTCs) comprise deposits from a range of weakly turbulent to fully cohesive, plug-like sediment gravity flows such as slides, slumps, and debris-flows (Talling et al., 2012). MTCs are one of the most sedimentological and seismically distinctive depositional elements in many deep-water depositional systems, where they may form a key component of the stratigraphic record (Posamentier and Martinsen, 2011). MTCs may represent geohazards, threatening seabed infrastructure, and can generate seabed topography that controls subsequent sediment dispersal patterns (Martinsen, 1989; Hühnerbach and Masson, 2004; Solheim et al., 2005; Lee et al., 2007; Sawyer, 2007; Urgeles and Camerlenghi, 2013; Kneller et al., 2016). In addition, MTCs may represent drilling hazards because of unpredictable intraformational pressures, and may form hydraulic seals to sandstone reservoirs (Piper et al., 1997; Shipp, 2004; Sawyer et al., 2009; Algar et al., 2011) or form reservoir themselves (Meckel III, 2011). The composition and distribution of MTCs, and our ability to recognise them in the subsurface, are thus of concern to the hydrocarbon industry.

MTCs are typically studied using seismic reflection (e.g. Prather et al., 1998; Posamentier and Kolla, 2003; Frey Martinez et al., 2005; Posamentier, 2005; Moscardelli et al., 2006; Moscardelli and Wood, 2008; Bull et al., 2009; Moernaut and De Batist, 2011; Ortiz-Karpf et al., 2015; Ortiz - Karpf et al., 2016), or outcrop data (e.g. Martinsen et al., 2003; Jackson and Johnson, 2009; Dykstra et al., 2011; King et al., 2011; Shipp et al., 2011; Alves, 2015; Sobiesiak et al., 2016; Hodgson et al., 2018). Seismic reflection data allow determination of the distribution, external geometry, internal structure, and kinematics of MTCs. However, these data do not provide a direct calibration of MTC lithology, which must instead be inferred from seismic facies analysis (Moscardelli et al., 2006; Madof et al., 2009; Perov and Bhattacharya, 2011). In contrast, outcrop-based studies permit detailed analysis of MTC structure and lithology, but these exhumed and weathered systems do not permit a direct petrophysical characterisation.

Petrophysical and lithological studies of buried MTCs are relatively rare, typically drawing on data collected from shallowly buried (<1400 m) deposits (e.g. Sawyer, 2007; Flemings et al., 2008; Sawyer et al., 2009; Algar et al., 2011; Dugan, 2012). These studies show that MTCs are very fine-grained, and are acoustically faster (and thus denser) and have higher resistivity (and

thus lower porosity) than surrounding, in-situ sediment of similar composition (Piper et al., 1997; Shipp, 2004; Sawyer, 2007; Algar et al., 2011; Dugan, 2012). How these properties vary with depth and how deeply-buried MTCs are expressed in petrophysical data at depths of interest to the hydrocarbon industry remains unknown. Using petrophysical data from offshore NW Borneo, Algar et al. (2011) studied several deeply buried MTCs; however, in this example they lacked access to high-resolution 3D seismic data to link seismic facies with petrophysical properties.

In this study, we use 3D seismic reflection and borehole data from the Atwater Valley concession of the northern Gulf of Mexico to investigate the relationship between the 3D seismic reflection and petrophysical expression of three deeply buried MTCs. By doing this, we can improve our ability to use such data to predict their subsurface rock properties and associated fluid flow behaviour.

2 Geological setting

Our study area is located in Block 8 of the Atwater Valley concession, c. 130 km SW of the modern Mississippi delta mouth, and c. 60 km basinward of the Pleistocene shelf edge (Galloway et al., 2000; Galloway, 2001) (Figure 1). Present water depths range from 1150 m in the SE to 650 m in the NW. The northern Mississippi slope comprises a series of salt diapirs and minibasins formed due to flow of the Jurassic Louann Salt (Martin and Bouma, 1982; Peel et al., 1995). This study focuses on Pleistocene sediments preserved within minibasins formed by subsidence into allochthonous salt (Jackson et al., 2018) (Figure 1). During the Early to Middle Pleistocene, the Mississippi River and its tributaries supplied the Mississippi delta, which delivered significant amounts of sediment to the shelf, slope, and basin-floor (Galloway et al., 2000; Galloway, 2008; Galloway et al., 2011). In the Late Pleistocene, the East Mississippi river merged with the Red River, forming a deeply incised, pro-glacial Mississippi valley (Saucier, 1997; Galloway et al., 2000). This valley, and the downdip Mississippi canyon, represented the main conduit for sediment transfer onto the basin floor (Weimer et al., 1998; Galloway et al., 2000; Winker and Booth, 2000).

A top salt depth map highlights the main salt structures and minibasins within the study area (Figure 2). This study focuses on the stratigraphic fill of an N-trending, up to 21 km long and 10 km wide minibasin that contains a 3.5 km thick succession of Plio-Pleistocene siliciclastics

(mini-basin 5; Figure 2). Biostratigraphic data provide a relatively low-resolution age control for the Cenozoic sediments (Figure 3B).

3 Dataset and Methods

The seismic dataset was acquired in 1995-1998, and reprocessed as a single survey in 2008. It contains a 3D zero-phase, Kirchhoff pre-stack depth-migrated seismic reflection volume, with a vertical sample rate of 10 m, record length of 15 km, and final bin size of 25m x 25 m. Vertical seismic resolution is 17-27 m. The dataset covers an area of approximately 550 km² in the southwestern Mississippi Canyon (MC) and northwestern Atwater Valley (AT) protraction areas of the east-central Gulf of Mexico (Figure 2). A slightly deviated exploration well (AT-8 #1 ST) was drilled in 1997 in the east of the study area, encountering a c. 3600 m-thick succession of Pleistocene deep-water clastic succession (Figure 2). The well-log dataset includes measurements of velocity (DT), gamma-ray (GR) and resistivity (RT); these data were calibrated with mud-log and seismic reflection data to infer the lithology and petrophysical properties of the MTCs and their bounding strata.

We mapped eight highly reflective, laterally continuous seismic horizons (H0 to seabed; Figure 3B), delineating MTCs preserved in minibasin 5. MTCs are imaged using a combination of variance and chaos seismic attribute maps. Variance and chaos attribute maps provide measurement of the discontinuities in seismic data, and are sensitive to stratigraphic and structural variability (Chopra and Marfurt, 2007; Brown, 2011). A seismic-to-well tie allowed the relationship between seismic facies and well-log facies to be determined, including the petrophysical properties of the MTCs. Five MTC-bearing intervals were drilled and logged by AT-8 #1 ST; we analyse three in this study (Figure 3B). Well-log data (i.e., GR, AC and RT) were used to infer the lithology of the MTCs and their bounding strata. Cross-plots were constructed to examine the petrophysical properties variation within MTC-bearing intervals and bounding strata.

4 Seismic facies analysis

A regional N-trending seismic profile through mini-basin 5 illustrates the geometry of the depocentre and bounding salt structures (Figure 3A). We see two main seismic reflection configurations: (i) *chaotic*, which are interpreted as MTCs (i.e. remobilised strata); and (ii)

continuous, which are interpreted as in-situ slope deposits (Figure 3C). The seismic facies characteristics of the MTCs (facies 3.1 and 3.2) and slope deposits (facies 1 and 2) are further classified based on a more detailed analysis of the seismic reflection characteristics, and by comparing their expression (e.g. reflectivity and continuity, and their external and internal geometry) with previous seismic facies analysis schemes developed for age-equivalent (i.e. Plio-Pleistocene) deep-water sediments deposited in nearby areas (Prather et al., 1998; Roesink et al., 2004; Sincavage et al., 2004; Madof et al., 2009; Doughty-Jones et al., 2017). The observed seismic facies, and their GR expression, are briefly described here and documented more fully in Table 1, before we provide a more detailed analysis of the petrophysical expression of the MTC-bearing intervals.

4.1 Seismic facies 1 (SF1)

SF1 comprises sub-parallel to parallel, moderate continuity, high-amplitude reflections. Typically, SF1 is ranging from c. 40-50 m thick, and has flat upper and lower contacts with bounding deposits (Table 1). In logs, SF1 has a blocky, low GR response at its base, and a serrated, higher GR response at its top, displaying an overall fining-upward trend. Based on its log response and previous seismic facies-based studies, we infer that SF1 represents thinly bedded, sandstone-rich (at its base) and mudstone-rich (at its top) deposits, possibly deposited in a channel-levee system or at the fringes of a lobe complex (Table 1). This is consistent with C_{th} facies of Prather et al. (1998), with similar seismic facies being documented by Roesink et al. (2004), Sincavage et al. (2004), and Madof et al. (2009) (i.e. inter-bedded sandstone- and mudstone-rich turbidites).

4.2 Seismic facies 2 (SF2)

SF2 is ranging from c. 100 m to 170 m thick, bounded by sub-parallel to parallel, relatively continuous, low-to-medium amplitude reflections and comprises laterally continuous, parallel, low- to medium amplitude reflections (Table 1). In log data, SF2 shows a high GR response, suggesting it is mudstone-dominated. Based on its expression in seismic and borehole data, and by comparison to seismic facies interpreted in previous studies, we interpreted SF2 as low-energy, mudstone-rich 'background' slope turbidite deposits and/or a mudstone-dominated hemipelagic drape (Prather et al., 1998; Madof et al., 2009; Perov and Bhattacharya, 2011).

4.3 Seismic facies 3.1 (SF3.1)

SF3.1 is ranging from c. 150-180 m thick, has a rugose top surface and a flat base (Table 1), and comprises moderately deformed, folded and faulted, medium-to-high amplitude seismic reflections. In log data, SF3.1 is expressed by a bell-shaped GR response, with a fining upward trend near its bottom, and box-shaped, 80-120 m thick intervals of low GR at its middle and top. We tie the lower part of SF3.1 with mudstone-rich deposit (i.e. high GR intervals), and the middle and upper parts with thick, sandstone-rich deposits, inter-bedded with thinly bedded mudstone (i.e. low GR intervals). The abundance of faulting and folding, combined with the rugose upper surface, suggest SF3.1 has been remobilised and transported within a MTC. However, based on previous seismic facies interpretations, which lack folding and faulting, and its log character, we interpret SF3.1 to represent sandstone-rich deposit that originally formed submarine lobes (Mahaffie, 1995; Prather et al., 1998; Posamentier and Kolla, 2003; Posamentier, 2005; Sawyer et al., 2007; Doughty-Jones et al., 2017).

4.3 Seismic facies 3.2 (SF3.2)

SF3.2 comprises c. 190-270 m thick packages of chaotic, low-to-moderate amplitude seismic reflections. The top of SF3.2 is rugose, whereas its basal contact is relatively flat (Table 1). In log data, SF3.2 is characterised by a serrated, overall high GR response that locally contains sharp-based, box-shaped, low GR intervals (Table 1). The lithology of SF3.2 is therefore interpreted as a mudstone-dominated succession (i.e. high GR intervals) that locally contains sandstone blocks (i.e. low GR intervals). Based on its seismic and log response, and interpretations arising from previous seismic facies-based studies (Prather et al., 1998; Sawyer, 2007; Madof et al., 2009; Perov and Bhattacharya, 2011), we interpret SF3.2 as a mudstone-rich debrite.

5. Lithology and distribution of MTCs

Minibasin 5 contains five main MTC-bearing intervals (Figure 3B, 3C); in this study, we focus on three representative examples, and we begin by providing a description of their general seismic expression and lithology. In subsequent sections, we synthesize observations from these three MTCs to investigate their detailed petrophysical response, and how this relates to MTC structure and emplacement.

5.1 MTC 1

Geometry and seismic facies

MTC 1 is bound by horizon H1 and H2 (Figure 3B). It has a tongue-shaped external form, widening SE away from diapir A (Figure 4A, 4B). MTC 1 is 270 m thick, and thickest in the minibasin centre. A 180 m high, 6 km long ramp separates MTC 1 from an overlying debrite (SF3.2), and an underlying interval that contains folded and faulted blocks (Figure 4C, 4D). The abundance of faulting and folding, combined with scours along the basal surface (Figure 4C), suggest that large blocks were transported within MTC1. These blocks are defined by packages of SF3.1 and SF1 that are 80-180 m thick, 4.5-6.8 km long, and 2-3.6 km wide, and which contain NE-SW-striking thrusts. The well intersects the distal part of MTC 1, where thrusts and folds occur (Figure 4A).

Lithology

MTC 1 is sandstone-rich (SF3.1) near its base and mudstone-rich (SF3.2) at its top (Figure 5A). To better investigate lithology variations associated with the three constituent seismic facies of MTC 1, we generated a cross-plot of shale volume (V_{sh}) and velocity (V_p) (Figure 5B). This plot shows that: (1) both SF1 and SF3.1 have similar proportions of sandstone-rich and mudstone-rich sediments; SF3.1 contains minor amounts of muddy sandstone, whereas SF1 does not; (2) sandstone-rich deposits associated with SF1 and SF3.1 are capped and surrounded by mudstone-rich debrite, an observation also inferred from seismic data (Figure 4C, 4D); (3) SF3.2 is mudstone-dominated, can be clearly differentiated from other seismic facies, and is defined by a relatively narrow range of distribution in the cross plot.

5.2 MTC 2

Geometry and seismic facies

We infer MTC 2 comprises two temporally separate, debrite-dominated (i.e. SF3.2) deposits (MTC 2.1 and 2.2; Figure 6A, 6B), separated by a through-going seismic horizon H2.2 (Figure 6C, 6D). Taken together, MTC 2.1 and 2.2 define an up to 120 m thick, N-trending, lenticular-shaped body that widens slightly towards the north (Figure 6B). Two bodies in the centre of the minibasin, and which have sharp, sub-vertical contacts with MTC 2.1, and are interpreted as remnant blocks (Figure 6C, 6D). The well interests the middle part of MTC 2 where it is dominated by chaotic seismic facies (Figure 6A).

Lithology

The remnant block is mudstone-rich at its base, and comprises sandstone and mudstone towards its top (Figure 7A). Overlying MTCs are mudstone-dominated (MTC 2.1 and 2.2; Figure 7A), although the lithological composition of MTC 2 varies when observed in the cross-plot of shale volume (Vsh) and velocity (Vp) (Figure 7B): (1) SF1 and SF3.2 are mudstone-dominated with a small portion of sandstone-rich deposits, although the former is, overall, more mudstone-rich than the latter; (2) SF2 is mudstone-rich, containing a small portion of muddy sandstone; (3) sandstone-rich deposits associated with SF1 are capped and surrounded by mudstone-rich debrite and undeformed background deposit; a similar stratigraphic relationship is inferred from the seismic data (Figure 6C, 6D).

5.3 MTC 3

Geometry and seismic facies

MTC 3 occurs in the centre of the minibasin, is slightly elongate, and trends north (Figure 8A, 8B). MTC 3 is bounded by horizon H4 and H4.1 (Figure 3B), is up to 182 m thick, comprises chaotic, moderate-amplitude reflections (SF3.2), and has a flat base and rugose top (Figure 8C, 8D). The well intersects the central part of MTC 3 where the region is dominated by chaotic seismic facies (Figure 8A).

Lithology

MTC 3 has a mudstone-rich base and top, and a sandstone-rich middle (Figure 9A). The lithological composition of MTC 3 is further revealed in a cross-plot of Vsh and Vp (Figure 9B). SF3.2 is dominated by sandstone-rich and mudstone-rich deposits, with a small portion of muddy sandstone. The lithology distribution in SF3.2 in MTC 3 is thus similar compared to the same seismic facies in MTC 2, but different to that in MTC 1. Based on seismic and log data, MTC 3 is interpreted as a debrite-dominated MTC containing large sandstone-rich (c. 70 m in thickness) blocks.

6 Petrophysical analysis of MTCs

6.1 General variations in velocity and resistivity

P-wave velocity (Vp) data from within MTCs 1-3 show that: (i) MTCs are generally characterised by an overall downward increase in Vp (e.g. 2340-2487 m, MTC3 in Figure 10A);

(ii) mudstone-dominated parts of MTCs are acoustically faster than similar lithologies at similar burial depths (e.g. the mudstone-rich debrite in MTC 3 is acoustically faster than the overlying and underlying background mudstone-rich deposits; 2300-2550 m in Figure 10A); (iii) sandstone-dominated parts of all three MTCs tend to have a relatively low V_p , and are acoustically slower than the overlying and underlying mudstone-rich debrite (see below); (iv) the lowermost 15-30 m of the MTCs, which are invariably mudstone-dominated and which directly overlie the basal shear surface, are 5%-9% and 7-25% acoustically faster than similar material within the overlying MTCs and underlying background deposits, respectively. We interpret this interval to represent the basal shear zone (BSZ), with the overall downward of increasing V_p likely to reflect increased compaction and density, and therefore velocity with depth (Figure 10A). The reasons for the sharp increase in V_p just above the MTC basal shear surface is discussed further below.

Resistivity (RT) log data show that: (i) RT increases downward within MTCs, but decreases downward in lithologically similar slope deposits in bounding intervals (e.g. increases from 2770-2890 m in MTC2, and decreases from 2890-3080 m in the underlying remnant block, Figure 10B); (ii) mudstone-rich debrite (SF3.2) are typically more resistive compared to surrounding, undeformed background deposits at similar burial depths (e.g., 3075-3100 m in MTC1 Figure 10B); (iii) sandstone-dominated parts of all three MTCs tend to have a relatively low RT, and are less resistive than overlying and underlying mudstone-rich debrite (see below); (iv) RT response within MTC 2 and MTC 3 are lower than surrounding, undeformed background deposits; and (v) the lowermost 15-30 m (BSZ) of MTCs are characterised by an RT value that is 15%-25% higher than would be expected by the downward-increasing, 'background' RT trend response in the overlying MTC, and 16%-30% higher than underlying and thus more deeply buried, slope background deposits (Figure 14). This finding is consistent with previous studies that suggest that RT increases with depth within MTCs (Shipp, 2004; Dugan, 2012), but is counter to other studies which suggest MTCs are typically more resistive than surrounding sediments (Sawyer et al., 2009; Algar et al., 2011). We explore the reasons for this further in the discussion.

6.2 Petrophysical and acoustic characteristics of the basal shear zone

The BSZs of all three MTCs are all characterised by negative, medium-to-high amplitude seismic reflections of moderate continuity (Figure 4D, 6C, 8C). For example, the BSZ of MTC 1

is more reflective (i.e. -15701 at point 'a' in Figure 11A) than the laterally correlative reflection within flanking background strata (i.e. -4008 at point 'b' in Figure 11A). Because amplitude (i.e. reflectivity) is a function of the reflection coefficient (RC) (i.e. acoustic impedance or 'AI' contrasts) and, ultimately, the acoustic properties of rocks, we can explore what lithological combination and/or variations in their physical properties (e.g. compaction) might give rise to the observed seismic response (equation 1):

$$RC = \frac{AI_2 - AI_1}{AI_2 + AI_1} \quad (1)$$

Where AI1 and AI2 are the sediments overlying and underlying the BSS of MTC 1, respectively (Figure 11B). Because the BSZ of MTC 1 is more consolidated, it is acoustically faster and more resistive than the underlying undeformed deposits (Figure 10A, 10B). AI is a function of acoustic velocity (Vp) and density (ρb) (equation 2):

$$AI = Vp * \rho b \quad (2)$$

Based on this, AI1>AI2 across the BSS of MTC 1. This illustrates why the amplitude of the BSZ of MTC 1 is not only defined by negative polarity, but is also brighter than that of the laterally correlative, undeformed background deposits.

6.3 Petrophysical and acoustic characteristics of sandstone-rich deposit within MTCs

MTC 1 has the thickest sandstone-rich interval (c. 170 m). Sandstone-rich intervals of MTC 2.1, 2.2 and 3 are up to 30 m, 10 m and 70 m thick, respectively (Table 2).

Overall, depth trends in sandstone-rich parts of the MTCs are more variable than in mudstone-rich parts. For example, in contrast to mudstone-rich parts of MTCs where Vp and RT broadly increase with depth (Figure 12A), sandstone-rich parts of MTCs have variable depth trends (Figure 12B). The sandstone-rich parts of three MTCs have lower average Vp and RT values than the mudstone-rich debrite above and below (Figure 13). For example, the average Vp of the sandstone-rich part in MTC 2 at 2140m/s is lower than the Vp of the overlying and underlying mudstone-rich debrites at 2210 m/s and 2240 m/s (Fig 13B). The sandstone-rich part of MTC 3 display an overall increase in Vp and RT with depth (Figure 13A), although the sandstone-rich part of MTC 1 does not vary in Vp and RT with depth (Figure 13C).

The petrophysical properties of sandstone-rich parts of MTC 1 are different to those of surrounding mudstone-rich debrite and sandstone-rich deposits in overlying, undeformed background deposits (Figure 13 C). A simplified Vp depth trend can be proposed based on the observed Vp depth trend in Figure 10A. The MTC intervals, except the sandstone-rich blocks in MTC 1, tend to have relatively high pore fluid pressures, which exceed the inferred hydrostatic pressure. This suggests that MTC intervals are more (over)compacted compared to overlying and underlying background slope deposits. Within MTC 1, the Vp trend of the sandstone-rich blocks shifts sharply to a constant low Vp response as compared to the overlying mudstone-rich debrite that has increasing Vp with depth. This indicates that the sandstone-rich blocks of MTC 1 are *less* compacted than the mudstone-rich, debritic matrix. Furthermore, sandstone-rich blocks are only weakly resistive when compared to the overlying mudstone-rich units (Figure 10, Figure 12, Figure 13C). This may suggest that the sandstone-rich blocks in MTC 1 retain higher porosity and are water-saturated.

7 Discussion

We have characterised: (i) the lithology of relatively deeply buried, seismic-scale MTCs; (ii) the relationship between MTC seismic facies and lithology; and (iii) the petrophysical properties of MTCs, and how they vary with depth and structural position within individual MTCs. Here, we discuss the key implications of our study.

7.1 Lithology of MTCs

In this study, we demonstrate that significant amounts of sandstone may be present within MTCs. This sandstone can be surprisingly thick (c. 170 m) and contained in relatively homogeneous transported blocks (SF3.2), or relatively thin (10-30 m) and interbedded with mudstone in remobilised lobe and/or channel-fill successions (Table 2). This compositional variability may reflect the different provenance of the MTCs; i.e. from mudstone-rich outer-shelves or slopes lacking sand, or from similar positions that are sandstone-rich due to the presence of deltas or previously deposited, deep-water channel-fills and lobes. This contrasts with the widespread occurrence of argillaceous MTCs, such as those encountered in the Nankai Trough (e.g. Strasser et al., 2012), offshore Angola (e.g. Sikkema and Wojcik, 2000) and in the Gulf of Mexico (e.g. Shipp, 2004; Flemings et al., 2005; Sawyer et al., 2007; Meckel III, 2011).

7.2 Petrophysical properties of MTCs

General Petrophysical properties

Prior well-log based studies from IODP and ODP drilling in the Northern Gulf of Mexico (Shipp et al., 2004; Sawyer, 2007; Sawyer et al., 2009; Dugan, 2012; Flemings et al., 2012) and Northwest Borneo (Algar et al., 2011) show that MTCs tend to have a higher Vp, density and RT values than surrounding non-MTC intervals. This reflects the fact that MTCs are more consolidated than their bounding sediments, an observation that is consistent with geotechnical measurements that indicate shear strength increases, whereas water content and void ratio decrease downward within MTCs (Piper et al., 1997; Shipp et al., 2004; Strong, 2009; Long et al., 2011; Alves et al., 2014). Physical experiments and theoretical models (e.g. consolidation, fluid-dynamics, and soil-mechanics) confirm that MTCs are denser than bounding strata, typically being densest along their basal shear zone (Major and Iverson, 1999; Sassa et al., 2003; Dugan and Germaine, 2008; Strong, 2009; Meissl et al., 2010).

We demonstrate that the three MTCs are more compacted than surrounding background deposits, and that Vp, RT broadly increase downward and with a higher rate as compared to the underlying and overlying un-deformed background sediments. Our findings are thus consistent with observations from Sawyer et al. (2009) and Algar et al. (2011), who show similar downward increase in Vp and RT within individual MTCs. However, RT values are lower than in underlying and overlying undeformed background sediments, except near the MTC basal shear surface. This observation is contrary to previous studies (Shipp, 2004; Sawyer et al., 2009; Dugan, 2012). These authors studied mudstone-dominated MTCs at relatively shallow burial depths (<1400 m), whereas those presented here are relatively sandstone-rich and lie at substantially greater burial depths (>2300 m). Therefore, the differences are attributed to differences in the burial depth and lithology of MTC intervals studied.

Insights into emplacement processes; basal shear surface or zone?

Experimental modelling based studies show that debrites are typically deposited in response to top-down 'freezing' of weakly turbulent, plug-like laminar flows; because the lower parts of these flows are the last to stop deforming they may be more strained (Pickering and Hiscott, 2015). Thin section and outcrop data based studies show evidence of liquefaction and fluidization related structures in the lower part of MTC intervals (Ogata et al., 2014). In this

study, we show that the lower 15-30 m of the studied MTCs are characterised by relatively high Vp and RT when compared to overlying and underlying deposits. Petrophysical data suggest that, rather than being underlain by a basal shear *surface*, the MTCs overlie basal shear *zone* (BSZ). BSZ thickness and infer strain (based on Vp value) appears to be positively correlated to the thickness of the overlying MTCs; i.e. the thicker the MTCs, the thicker and more strained the BSZs. For example, MTC 3 and MTC 2 are 170 and 83 m thick, with 30 m and 26 m thick BSZs, respectively. Vp values sharply increase at the BSZs by around 20-25% for each MTC, as compared to the overlying debritic sediments of the main MTC body. This contrasts with MTC 1, where the BSZ is only 15 m thick and where Vp increases by only 7%. These differences in Vp may reflect the fact that the well: (i) penetrates different parts of the different MTCs (i.e. the margin of MTC 1 vs. the centre of MTCs 2 and 3), and (ii) penetrates different types of the MTCs (i.e. transported blocks in MTC 1 and debris flow matrix in MTCs 2 and 3).

Although only one well is available for this analysis, some observations can be made with respect to lateral variability of petrophysical properties (i.e. Vp and RT) within the MTCs. Vp and the thickness of the BSZs appear to vary laterally, being highest beneath the main body of an MTC (i.e. MTC 2 and MTC 3), and lowest in more distal parts (i.e. MTC 1). This suggests that within a single MTC, the BSZ might be thinnest along its margins and thickest beneath its body. However, the thickness and pore pressure of the BSZ might be controlled by other factors, such as: (i) slope angle, which would dictate the momentum of MTCs towards the underlying substrate (i.e. the steeper slope angle, the higher the momentum, and *vice versa*; Algar et al., 2011); (ii) the thickness of the overlying MTC (i.e. BSZ thickness is proportional to the thickness of the overlying MTCs; e.g., MTC 3 is thicker than MTC2, and thus the thickness of BSZ of the former is thicker than that of the latter); (iii) MTC transport mode; the MTCs with fewer blocks (i.e. MTC 2 and 3) will have a thicker BSZs than the MTCs with more transported blocks (MTC 1); (iv) the lithology of the underlying substrate; i.e. a ductile, mudstone-rich substrate may be highly sheared, with the shear stress from the overlying MTCs leading to dewatering rather than erosion of the BSZ (Alves and Lourenço, 2010; Ortiz-Karpf et al., 2017); and (v) bathymetric confinement, which would influence the substrate geometry, heterogeneity, internal characteristics and pathway of MTCs; the thickness of MTCs and their BSZ would thus vary laterally (Ortiz-Karpf et al., 2017).

In detail, we suggest the inferred high shear strain characterising the BSZs reflect three stages during MTC emplacement (Figure 14a, b): (i) Phase 1 – high shear stresses within the BSZs cause an increase in fluid pressure beneath the rapidly deposited very fine-grained upper part of the flow; this drives liquefaction within the BSZ (Figure 14c); (ii) Phase 2 – continued shearing drives fluidization and pore fluid expulsion (Figure 14d); and (iii) Phase 3 - as gravity induced shear stress progresses, fluid escape continues to happen, resulting in reduction of pore spaces which then makes the BSZ more compacted (Figure 14e). A key observation is that, even where 30 m thick, the BSZs are too thin to be recognised in seismic reflection data (i.e. these intervals are sub-seismic).

Identifying MTCs using petrophysical data

On the middle to lower slope of the Mississippi fan, GR log data cannot differentiate between MTCs and undeformed background deposits because both are mudstone-rich (i.e. both are characterised by serrated, overall high-GR responses). In this situation, Vp and RT logs may be more useful, as they may present higher values in the MTC debrite than the background deposits, principally because these deposits have undergone some degree of transport, and thus emplacement-related strain and compaction. Our method, which may allow well-based, petrophysically driven mapping of MTCs and their BSZs, can be used in lower-quality 3D seismic datasets that image deep-water sedimentary successions (e.g. sub-salt-canopy minibasins within which seismic resolution is relatively low).

7.3 Petroleum implication of MTCs

MTCs as hydrocarbon seals

Most petrophysics-based studies of MTCs indicate these deposits are dominated by mudstone. Furthermore, these studies suggest that, because they are over-compacted, these mudstone-rich MTCs may be better seals than surrounding deposits (Algar et al., 2011). This study suggests that emplacement-related over-compaction in MTCs occurs within the BSZ, meaning this interval may have higher sealing potential than lithologically similar background deposits occurring at similar burial depths. The highly reflective nature of the BSZ of an MTC, which relates to its higher density and acoustic velocity, may thus be an indicator of higher seal potential. The mudstone-rich debrite in the upper part of MTC 1 appears to be a good top and lateral seal for the underlying folded and faulted sandstone-rich transported blocks

(Figure 4C, 4D). In MTC 2, the mudstone-rich debrite (MTC 2.1 and MTC 2.2) and the corresponding BSZ may act as a good top and lateral seal for the underlying, sandstone-rich parts of the remnant block (Figure 6C, 6D). In BSZ of MTC 3, which appears to be the most consolidated of all the recognised BSZs, could act as good base seal for underlying sandstone-rich deposits.

Reservoir potential

In this study, we show that sandstone-rich transported blocks can be up to c. 180 m thick, 6800 m long, cover 2.5 km² in map-view, and have an approximate volume of 4.5 km³ (i.e. MTC 1). The sandstone-rich parts within remnant blocks underlying MTC 2 are up to 20 m thick, cover 0.0145 km² in map-view, and have an approximate volume of 0.29 km³. Petrophysical data indicate the sandstone-rich blocks within MTC 1 and in the remnant block might be under-pressured and may thus be characterised by relatively high porosities. These transported yet less-deformed sandstone-rich blocks (i.e. MTC 1), and the sandstone-rich parts within the remnant blocks under MTC 2, could be potential reservoirs and may thus be of interest to the hydrocarbon industry (Moore et al., 1995; Alves, 2010; Dunlap et al., 2010; Principaud et al., 2015). In addition and as stated above, the sandstone-rich parts within MTC 1 and the remnant blocks are capped by the overlying mudstone-rich deposit, and are externally sealed by the surrounding, mudstone-rich background strata. Intra-MTC blocks of comparable size to those described here (i.e. 1-10 km long, 0.3-2 km wide, 50-500 m thick, and covering an area of 3.63-4 km² have been described by other workers, (e.g., Moscardelli et al., 2006; Ogiesoba and Hammes, 2012).

8. Conclusions

The petrophysical data and seismic reflection character of three MTCs preserved in a minibasin in the northern Gulf of Mexico indicate that: (i) MTCs are dominated by chaotic, medium-to-low amplitude seismic reflections (debrite), and packages of deformed, but more continuous, medium-to-high amplitude reflections (remnant and transported blocks); (ii) petrophysical data indicate the MTCs are mudstone-dominated, whereas the transported and remnant blocks are relatively sandstone-rich; (iii) MTCs are characterised by high acoustic velocities (as revealed by Vp data) and are relatively more resistive relative to surrounding background sediments at similar burial depths; (iv) the lowermost 15-30 m of the MTCs

comprises basal shear zones, which are characterised by relatively high P-wave velocity (V_p) and resistivity (RT) values due to shear-induced over-compaction; (v) V_p and RT vary laterally within the BSZs, being highest in main body of MTC and lower towards the margins; (vi) the hydrocarbon seal potential of MTCs may be internally highly variable, with the BSZ displaying the greatest seal capacity (smallest pore throat diameter and lowest permeability) towards the main body of the MTCs compared to the deposit margins; and (vii) sandstone-rich blocks within the MTC 1 tend to be under-compacted and may maintain anomalously high porosities. Sandstone-rich blocks tend to be internally sealed by overlying mudstone-rich debris and externally sealed by background mudstone-rich deposits.

Acknowledgements

We thank PGS, in particular Don Herron and Scott Opdyke, for providing the subsurface dataset and allowing the publication of the paper. We would also thank to Harya Nugraha and Michael Steventon who helped us throughout the work.

Figure captions

Figure 1. Location map of the study area (red box), showing the position of the modern shelf edge (black dotted line), paleo-shelf edge (white dotted line), and modern depositional systems.

Figure 2. Depth map for top salt, showing the overall salt-tectonic structure of the study area. 1-5 and A-C refer to minibasins and salt structures, respectively, described in the text.

Figure 3. (A) N-trending seismic section showing the overall salt-tectonic structure of the study area. (B) The eight key seismic horizons (H0 to seabed) and main MTC-bearing intervals. (C) The main seismic facies and depositional element interpretation. See Figure 2 for the location of the seismic line. Note the position of well AT-8 #1 ST.

Figure 4. (A) Variance map between horizon H1 and 2. The red dot indicates the well location; A-C are salt diapirs referred to in the text. (B) Sketch of MTC 1 indicating some of the key internal structures. Note: (i) the ramp; (ii) the MTC lateral margin; (iii) salt-related normal faults, (iv) intra-MTC thrusts; and (v) transported blocks. (C) WNW-trending seismic profile showing the range of seismic facies within MTC 1 (see figure 4A for location). (D) ENE-trending seismic profile showing the range of seismic facies within MTC 1 (see figure 4A for location).

Figure 5. (A) Wireline logs, interpreted lithology, and extracted seismic reflection of MTC 1. Log tracks are gamma ray, acoustic (DTCO1), resistivity (ATR1), lithology interpreted by gamma ray and acoustic log. (B) V_{shale} (V_{sh}) against Velocity (V_p) cross plot for three seismic facies associations within MTC 1. Each seismic facies tend to plot in a distinct cluster with however some dots are plotting away from correlated cluster. Note in Fig. 5A the black dashed lines are top and base boundaries of MTC1, and the black dotted lines are boundaries of each seismic facies. DTCO stands for Delta-Time Compressional (microsec/ft), ATR stands for Attenuation resistivity (deep; ohm-m). The depth is in measured depth.

Figure 6. (A) Variance map between horizon H2 and 2.1. The red dot indicates the well location; A-C are salt diapirs referred to in the text. (B) Sketch of MTC 2 indicating some key structures and features. Note: (i) the remnant block, (ii) salt-related normal faults, and (iii) lateral margin. (C) NNE-trending seismic profile showing the range of seismic facies within MTC 2 (see figure

4.1 for location). (D) WWE-trending seismic profile showing the range of seismic facies within MTC 2 (see figure 6A for location). The depth is in measured depth.

Figure 7. Wireline logs, interpreted lithology, and extracted seismic reflection of MTC 2. Log tracks are gamma ray, acoustic (DTCO1), resistivity (ATR1), lithology interpreted by gamma ray and acoustic log. (B) V_{shale} (Vsh) against Velocity (V_p) cross plot for three seismic facies associations within MTC 2. Each seismic facies tend to plot in a distinct cluster with however some dots are plotting away from correlated cluster. Note in Fig. 7A the black dashed lines are top and base boundaries of MTC2, and the black dotted lines are boundaries of each seismic facies. DTCO stands for Delta-Time Compressional (microsec/ft), ATR stands for Attenuation resistivity (deep; ohm-m). The depth is in measured depth.

Figure 8. (A) Chaos map between horizon 4 and horizon 4.1. The red dot indicates the well location; A-C are salt diapirs referred to in the text. (B) Sketch of MTC 3 indicating some key structures and features. Note: (i) the remnant block, (ii) salt-related normal faults, and (iii) lateral margin. (C) WWE-trending seismic profile showing the range of seismic facies within MTC 3 (see figure 8A for location). (D) WWE-trending seismic profile showing the range of seismic facies within MTC 3 (see figure 8A for location). The depth is in measured depth

Figure 9. (A) Wireline logs and interpreted lithology of MTC 3. Log tracks are gamma ray, acoustic (DTCO1), resistivity (ATR1), lithology interpreted by gamma ray and acoustic log, and extracted seismic reflection. Note the black dashed lines are top and bottom boundaries of MTC1, black dotted lines are boundaries of each seismic facies. DTCO stands for Delta-Time Compressional (microsec/ft), ATR stands for Attenuation resistivity (deep; ohm-m). (B) V_{shale} against Velocity cross plot for seismic facies 3.2 associations within MTC 3. The depth is in measured depth.

Figure 10. (A) Velocity (V_p) log, interpreted lithology column, and a schematic sketch of V_p depth trend. (B) Resistivity (R_t) log and interpreted lithology column. Note that the dotted black line in Figure 10A indicates inferred hydrostatic trend based on V_p log.

Figure 11. (A) Amplitude map extracted at basal shear surface of MTC 1 and its correlative surface underlying undeformed strata. Bright amplitude occurs when MTC 1 overlays the surface, and dim amplitude corresponds to the surface underlying undeformed substrate. (B)

Schematic cross-section of MTC 1 and its correlative undeformed strata, see location from figure 11A.

Figure 12. (A) Velocity (V_p) and Resistivity (R_t) logs of mudstone-rich deposits covering background and MTC deposits. (B) Velocity (V_p) and Resistivity (R_t) logs of sandstone-rich deposits covering background and MTC deposits.

Figure 13. (A) Velocity (V_p) and Resistivity (R_t) logs of MTC 3. (B) Velocity (V_p) and Resistivity (R_t) logs of MTC 2. (C) Velocity (V_p) and Resistivity (R_t) logs of MTC 1, see the depth interval from Velocity (V_p) log in Figure 10.

Figure 14 a) Schematic sketch of MTC and its basal shear zone; b) schematic sketch of V_p and R_t logs within MTC intervals. Schematic sketch of processes within the basal shear zone (see location in a): liquefaction (c); fluid escape (d); overcompaction (e).

Table captions

Table 1 Summary of seismic facies in minibasin 5, including well logs, lithology, schematic facies geometries, facies characteristics, and depositional environment.

Table 2 Approximate dimensions of MTCs by log mapping.

Reference

- Algar, S., Milton, C., Upshall, H., Roestenburg, J., and Crevello, P., 2011, Mass-transport deposits of the deepwater northwestern Borneo margin (Malaysia)—Characterization from seismic-reflection, borehole, and core data with implications for hydrocarbon exploration and exploitation: Mass-transport deposits in deepwater settings: Tulsa, Oklahoma, SEPM Special Publication, v. 96, p. 351-366.
- Alves, T. M., 2010, 3D seismic examples of differential compaction in mass-transport deposits and their effect on post-failure strata: *Marine Geology*, v. 271, no. 3, p. 212-224.
- , 2015, Submarine slide blocks and associated soft-sediment deformation in deep-water basins: a review: *Marine and Petroleum Geology*, v. 67, p. 262-285.
- Alves, T. M., Kurtev, K., Moore, G. F., and Strasser, M., 2014, Assessing the internal character, reservoir potential, and seal competence of mass-transport deposits using seismic texture: A geophysical and petrophysical approach: *AAPG bulletin*, v. 98, no. 4, p. 793-824.
- Alves, T. M., and Lourenço, S. D., 2010, Geomorphologic features related to gravitational collapse: Submarine landsliding to lateral spreading on a late Miocene–Quaternary slope (SE Crete, eastern Mediterranean): *Geomorphology*, v. 123, no. 1-2, p. 13-33.
- Brown, A. R., 2011, Interpretation of three-dimensional seismic data, Society of Exploration Geophysicists and American Association of Petroleum Geologists.
- Bull, S., Cartwright, J., and Huuse, M., 2009, A review of kinematic indicators from mass-transport complexes using 3D seismic data: *Marine and Petroleum Geology*, v. 26, no. 7, p. 1132-1151.
- Chopra, S., and Marfurt, K. J., 2007, Seismic attributes for prospect identification and reservoir characterization, Society of Exploration Geophysicists and European Association of Geoscientists and Engineers.
- Doughty-Jones, G., Mayall, M., and Lonergan, L., 2017, Stratigraphy, facies, and evolution of deep-water lobe complexes within a salt-controlled intraslope minibasin: *AAPG Bulletin*, v. 101, no. 11, p. 1879-1904.
- Dugan, B., 2012, Petrophysical and consolidation behavior of mass transport deposits from the northern Gulf of Mexico, IODP Expedition 308: *Marine Geology*, v. 315, p. 98-107.
- Dugan, B., and Germaine, J. T., 2008, Near - seafloor overpressure in the deepwater Mississippi Canyon, northern Gulf of Mexico: *Geophysical Research Letters*, v. 35, no. 2.
- Dunlap, D. B., Wood, L. J., Weisenberger, C., and Jabour, H., 2010, Seismic geomorphology of offshore Moroccos east margin, Safi Haute Mer area: *AAPG bulletin*, v. 94, no. 5, p. 615-642.
- Dykstra, M., Garyfalou, K., Kertzus, V., Kneller, B., Milana, J., Molinaro, M., Szuman, M., and Thompson, P., 2011, Mass-transport deposits: combining outcrop studies and seismic forward

- modeling to understand lithofacies distributions, deformation, and their seismic expression: Mass-Transport Deposits. SEPM, Tulsa, OK.
- Flemings, P., Long, H., Dugan, B., Germaine, J., John, C., Behrmann, J. H., Sawyer, D., and Expedition, I., 2008, Pore pressure penetrometers document high overpressure near the seafloor where multiple submarine landslides have occurred on the continental slope, offshore Louisiana, Gulf of Mexico: *Earth and Planetary Science Letters*, v. 269, no. 3, p. 309-325.
- Flemings, P. B., Behrmann, I., Davies, T., John, C., and Team, E., 2005, Gulf of Mexico hydrogeology— Overpressure and fluid flow processes in the deepwater Gulf of Mexico: Slope stability, seeps, and shallow-water flow: *Integrated Ocean Drilling Program Scientific Prospectus*, v. 308, p. 1-52.
- Flemings, P. B., John, C., and Behrmann, J., 2012, Expedition 308 synthesis: overpressure, consolidation, and slope stability on the continental slope of the Gulf of Mexico.
- Frey Martinez, J., Cartwright, J., and Hall, B., 2005, 3D seismic interpretation of slump complexes: examples from the continental margin of Israel: *Basin Research*, v. 17, no. 1, p. 83-108.
- Galloway, W. E., 2001, Cenozoic evolution of sediment accumulation in deltaic and shore-zone depositional systems, northern Gulf of Mexico Basin: *Marine and Petroleum Geology*, v. 18, no. 10, p. 1031-1040.
- , 2008, Depositional evolution of the Gulf of Mexico sedimentary basin: *Sedimentary basins of the world*, v. 5, p. 505-549.
- Galloway, W. E., Ganey-Curry, P. E., Li, X., and Buffler, R. T., 2000, Cenozoic depositional history of the Gulf of Mexico basin: *AAPG bulletin*, v. 84, no. 11, p. 1743-1774.
- Galloway, W. E., Whiteaker, T. L., and Ganey-Curry, P., 2011, History of Cenozoic North American drainage basin evolution, sediment yield, and accumulation in the Gulf of Mexico basin: *Geosphere*, v. 7, no. 4, p. 938-973.
- Hodgson, D., Brooks, H., Ortiz-Karpf, A., Spychala, Y., Lee, D., and Jackson, C.-L., 2018, Entrainment and abrasion of megaclasts during submarine landsliding and their impact on flow behaviour: *Geological Society, London, Special Publications*, v. 477, p. SP477. 426.
- Hühnerbach, V., and Masson, D., 2004, Landslides in the North Atlantic and its adjacent seas: an analysis of their morphology, setting and behaviour: *Marine Geology*, v. 213, no. 1-4, p. 343-362.
- Jackson, C. A.-L., Zhang, Y., Herron, D. A., and Fitch, P. J., 2018, Subsurface expression of a tertiary salt weld, Gulf of Mexico: *Petroleum Geoscience*, p. petgeo2018-2008.

- Jackson, C. A., and Johnson, H. D., 2009, Sustained turbidity currents and their interaction with debrite-related topography; Labuan Island, offshore NW Borneo, Malaysia: *Sedimentary Geology*, v. 219, no. 1-4, p. 77-96.
- King, P. R., Ilg, B. R., Arnot, M., Browne, G. H., Strachan, L. J., Crundwell, M., Helle, K., Shipp, R., Weimer, P., and Posamentier, H., 2011, Outcrop and seismic examples of mass-transport deposits from a late Miocene deep-water succession, Taranaki Basin, New Zealand: *Mass-transport deposits in deepwater settings: Society for Sedimentary Geology (SEPM) Special Publication 96*, p. 311-347.
- Kneller, B., Dykstra, M., Fairweather, L., and Milana, J. P., 2016, Mass-transport and slope accommodation: implications for turbidite sandstone reservoirs: *AAPG Bulletin*, v. 100, no. 2, p. 213-235.
- Lee, H. J., Locat, J., Desgagnés, P., Parsons, J. D., McAdoo, B. G., Orange, D. L., Puig, P., Wong, F. L., Dartnell, P., and Boulanger, E., 2007, Submarine mass movements on continental margins, *Continental margin sedimentation: from sediment transport to sequence stratigraphy*, Volume 37, Citeseer, p. 213-274.
- Long, H., Flemings, P., Germaine, J., and Saffer, D., 2011, Consolidation and overpressure near the seafloor in the Ursa Basin, Deepwater Gulf of Mexico: *Earth and Planetary Science Letters*, v. 305, no. 1, p. 11-20.
- Madof, A. S., Christie-Blick, N., and Anders, M. H., 2009, Stratigraphic controls on a salt-withdrawal intraslope minibasin, north-central Green Canyon, Gulf of Mexico: Implications for misinterpreting sea level change: *AAPG bulletin*, v. 93, no. 4, p. 535-561.
- Mahaffie, M., 1995, Reservoir classification for turbidite intervals at the Mars discovery, Mississippi Canyon Block 807, Gulf of Mexico.
- Major, J. J., and Iverson, R. M., 1999, Debris-flow deposition: Effects of pore-fluid pressure and friction concentrated at flow margins: *Geological Society of America Bulletin*, v. 111, no. 10, p. 1424-1434.
- Martin, R. G., and Bouma, A. H., 1982, Active diapirism and slope steepening, northern Gulf of Mexico continental slope: *Marine Georesources & Geotechnology*, v. 5, no. 1, p. 63-91.
- Martinsen, O., 1989, Styles of soft-sediment deformation on a Namurian (Carboniferous) delta slope, Western Irish Namurian Basin, Ireland: *Geological Society, London, Special Publications*, v. 41, no. 1, p. 167-177.
- Martinsen, O. J., Lien, T., Walker, R. G., and Collinson, J. D., 2003, Facies and sequential organisation of a mudstone-dominated slope and basin floor succession: the Gull Island Formation, Shannon Basin, Western Ireland: *Marine and Petroleum Geology*, v. 20, no. 6-8, p. 789-807.

- Meckel III, L., 2011, Reservoir characteristics and classification of sand-prone submarine mass-transport deposits: SEPM Special Publication, v. 96, p. 432-452.
- Meissl, S., Behrmann, J., and Behrmann, J. H., Data report: preliminary assessment of Pleistocene sediment strength in the Ursa Basin (Gulf of Mexico continental slope) from triaxial and ring shear test data, *in* Proceedings Proceedings of the Integrated Ocean Drilling Program 2010, Volume 308.
- Moernaut, J., and De Batist, M., 2011, Frontal emplacement and mobility of sublacustrine landslides: results from morphometric and seismostratigraphic analysis: *Marine Geology*, v. 285, no. 1-4, p. 29-45.
- Moore, J. G., Bryan, W. B., Beeson, M. H., and Normark, W. R., 1995, Giant blocks in the South Kona landslide, Hawaii: *Geology*, v. 23, no. 2, p. 125-128.
- Moscardelli, L., and Wood, L., 2008, New classification system for mass transport complexes in offshore Trinidad: *Basin Research*, v. 20, no. 1, p. 73-98.
- Moscardelli, L., Wood, L., and Mann, P., 2006, Mass-transport complexes and associated processes in the offshore area of Trinidad and Venezuela: *AAPG bulletin*, v. 90, no. 7, p. 1059-1088.
- Ogata, K., Mountjoy, J., Pini, G. A., Festa, A., and Tinterri, R., 2014, Shear zone liquefaction in mass transport deposit emplacement: A multi-scale integration of seismic reflection and outcrop data: *Marine Geology*, v. 356, p. 50-64.
- Ogiesoba, O., and Hammes, U., 2012, Seismic interpretation of mass-transport deposits within the upper Oligocene Frio Formation, south Texas Gulf Coast: *AAPG bulletin*, v. 96, no. 5, p. 845-868.
- Ortiz-Karpf, A., Hodgson, D., and McCaffrey, W., 2015, The role of mass-transport complexes in controlling channel avulsion and the subsequent sediment dispersal patterns on an active margin: the Magdalena Fan, offshore Colombia: *Marine and Petroleum Geology*, v. 64, p. 58-75.
- Ortiz-Karpf, A., Hodgson, D. M., Jackson, C. A.-L., and McCaffrey, W. D., 2017, Influence of Seabed Morphology and Substrate Composition On Mass-Transport Flow Processes and Pathways: Insights From the Magdalena Fan, Offshore Colombia: *Journal of Sedimentary Research*, v. 87, no. 3, p. 189-209.
- Ortiz - Karpf, A., Hodgson, D. M., Jackson, C. A. L., and McCaffrey, W. D., 2016, Mass - Transport Complexes as Markers of Deep - Water Fold - and - Thrust Belt Evolution: Insights from the Southern Magdalena Fan, Offshore Colombia: *Basin Research*.
- Peel, F., Travis, C., and Hossack, J., 1995, Genetic structural provinces and salt tectonics of the Cenozoic offshore US Gulf of Mexico: A preliminary analysis.

- Perov, G., and Bhattacharya, J. P., 2011, Pleistocene shelf-margin delta: Intradeltaic deformation and sediment bypass, northern Gulf of Mexico: AAPG bulletin, v. 95, no. 9, p. 1617-1641.
- Pickering, K., and Hiscott, R., 2015, Deep Marine Systems: Processes, Deposits, Environments, Tectonic and Sedimentation, John Wiley & Sons.
- Piper, D., Pirmez, C., Manley, P., Long, D., Flood, R., Normark, W., and Showers, W., Mass-transport deposits of the Amazon Fan, *in* Proceedings PROCEEDINGS-OCEAN DRILLING PROGRAM SCIENTIFIC RESULTS1997, NATIONAL SCIENCE FOUNDATION, p. 109-146.
- Posamentier, H. W., 2005, Stratigraphy and geomorphology of deep-water mass transport complexes based on 3D seismic data, SEG Technical Program Expanded Abstracts 2005, Society of Exploration Geophysicists, p. 2300-2303.
- Posamentier, H. W., and Kolla, V., 2003, Seismic geomorphology and stratigraphy of depositional elements in deep-water settings: Journal of sedimentary research, v. 73, no. 3, p. 367-388.
- Posamentier, H. W., and Martinsen, O. J., 2011, The character and genesis of submarine mass-transport deposits: insights from outcrop and 3D seismic data: Mass-transport deposits in deepwater settings: Society for Sedimentary Geology (SEPM) Special Publication 96, p. 7-38.
- Prather, B. E., Booth, J. R., Steffens, G. S., and Craig, P. A., 1998, Classification, lithologic calibration, and stratigraphic succession of seismic facies of intraslope basins, deep-water Gulf of Mexico: AAPG bulletin, v. 82, no. 5, p. 701-728.
- Principaud, M., Mulder, T., Gillet, H., and Borgomano, J., 2015, Large-scale carbonate submarine mass-wasting along the northwestern slope of the Great Bahama Bank (Bahamas): Morphology, architecture, and mechanisms: Sedimentary Geology, v. 317, p. 27-42.
- Roesink, J. G., Weimer, P., and Bouroullec, R., 2004, Sequence stratigraphy of Miocene to Pleistocene sediments of east-central Mississippi canyon, northern Gulf of Mexico.
- Sassa, S., Miyamoto, J., and Sekiguchi, H., 2003, The dynamics of liquefied sediment flow undergoing progressive solidification, Submarine Mass Movements and Their Consequences, Springer, p. 95-102.
- Saucier, R. T., 1997, Geomorphology and Quarternary Geologic History of the Lower Mississippi Valley. Volume 1.
- Sawyer, D. E., 2007, Lateral Variations in Core, Log, and Seismic Attributes of a Mass Transport Complex in the Ursa Region, IODP Expedition 308, Northern Gulf of Mexico.
- Sawyer, D. E., Flemings, P. B., Dugan, B., and Germaine, J. T., 2009, Retrogressive failures recorded in mass transport deposits in the Ursa Basin, Northern Gulf of Mexico: Journal of Geophysical Research: Solid Earth, v. 114, no. B10.

- Sawyer, D. E., Flemings, P. B., Shipp, R. C., and Winker, C. D., 2007, Seismic geomorphology, lithology, and evolution of the late Pleistocene Mars-Ursa turbidite region, Mississippi Canyon area, northern Gulf of Mexico: AAPG bulletin, v. 91, no. 2, p. 215-234.
- Shipp, R. C., 2004, Physical Characteristics and Impact of Mass Transport Complexes on Deepwater Jetted Conductors and Suction Anchor Piles.
- Shipp, R. C., Nott, J. A., and Newlin, J. A., Physical characteristics and impact of mass transport complexes on deepwater jetted conductors and suction anchor piles, *in* Proceedings Offshore Technology Conference 2004, Offshore Technology Conference.
- Shipp, R. C., Weimer, P., and Posamentier, H. W., 2011, Mass-transport deposits in deepwater settings, SEPM Soc for Sed Geology, v. 96.
- Sikkema, W., and Wojcik, K. M., 2000, 3D Visualization of Turbidite Systems, Lower Congo Basin, Offshore Angola, *in* Weimer, P., ed., Deep-Water Reservoirs of the World, SEPM Society for Sedimentary Geology.
- Sincavage, R., Weimer, P., and Bouroullec, R., 2004, Sequence Stratigraphy of Upper-Miocene to Pleistocene Sediments of Southwestern Mississippi Canyon and Northwestern Atwater Valley, Northern Gulf of Mexico.
- Sobiesiak, M. S., Kneller, B., Alsop, G. I., and Milana, J. P., 2016, Internal deformation and kinematic indicators within a tripartite mass transport deposit, NW Argentina: Sedimentary Geology.
- Solheim, A., Bryn, P., Sejrup, H., Mienert, J., and Berg, K., 2005, Ormen Lange—an integrated study for the safe development of a deep-water gas field within the Storegga Slide Complex, NE Atlantic continental margin; executive summary, Ormen Lange—an Integrated Study for Safe Field Development in the Storegga Submarine Area, Elsevier, p. 1-9.
- Strasser, M., Henry, P., Kanamatsu, T., Thu, M. K., Moore, G. F., and Expedition, I., 2012, Scientific drilling of mass-transport deposits in the Nankai accretionary wedge: First results from IODP Expedition 333, Submarine mass movements and their consequences, Springer, p. 671-681.
- Strong, H. E., 2009, The origin and properties of mass transport deposits, Ursa Basin, Gulf of Mexico.
- Talling, P. J., Masson, D. G., Sumner, E. J., and Malgesini, G., 2012, Subaqueous sediment density flows: Depositional processes and deposit types: Sedimentology, v. 59, no. 7, p. 1937-2003.
- Urgeles, R., and Camerlenghi, A., 2013, Submarine landslides of the Mediterranean Sea: Trigger mechanisms, dynamics, and frequency - magnitude distribution: Journal of Geophysical Research: Earth Surface, v. 118, no. 4, p. 2600-2618.
- Weimer, P., Varnai, P., Budhijanto, F. M., Acosta, Z. M., Martinez, R. E., Navarro, A. F., Rowan, M. G., McBride, B. C., Villamil, T., and Arango, C., 1998, Sequence stratigraphy of Pliocene and

Pleistocene turbidite systems, northern Green Canyon and Ewing Bank (offshore Louisiana), northern Gulf of Mexico: AAPG bulletin, v. 82, no. 5, p. 918-960.

Winker, C. D., and Booth, J. R., Sedimentary dynamics of the salt-dominated continental slope, Gulf of Mexico: integration of observations from the seafloor, near-surface, and deep subsurface, *in* Proceedings GCSSEPM Foundation 20th Annual Research Conference, Deep-Water Reservoirs of the World2000, SEPM, p. 1059-1086.

Figure 1

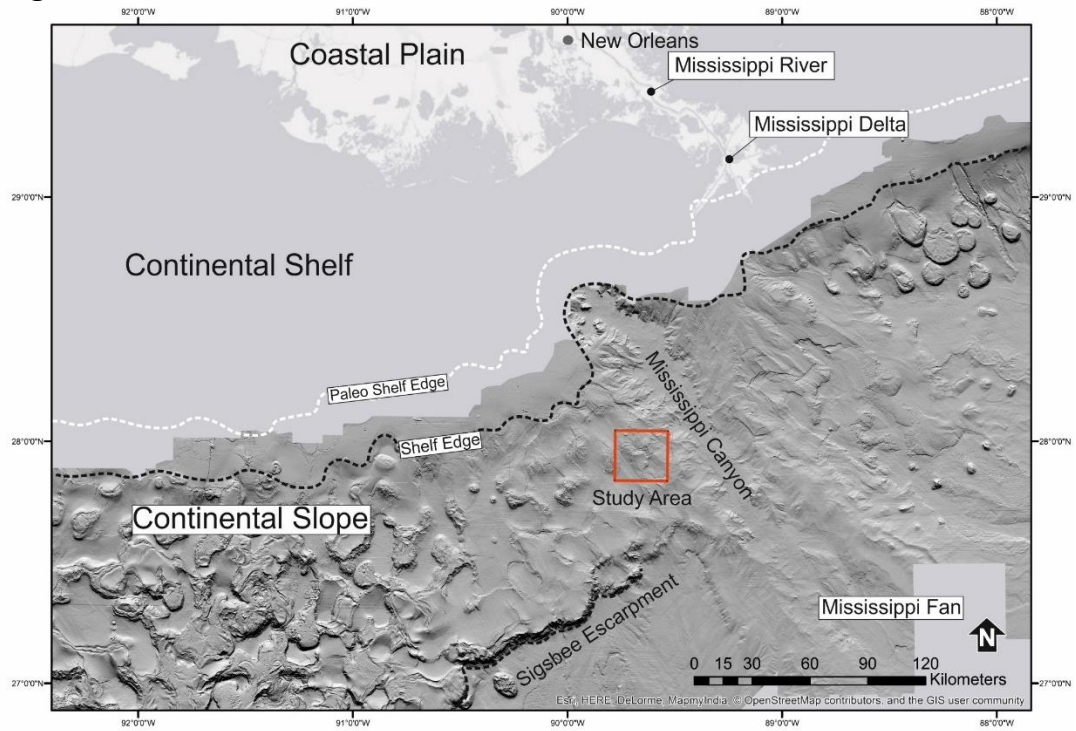


Figure 2

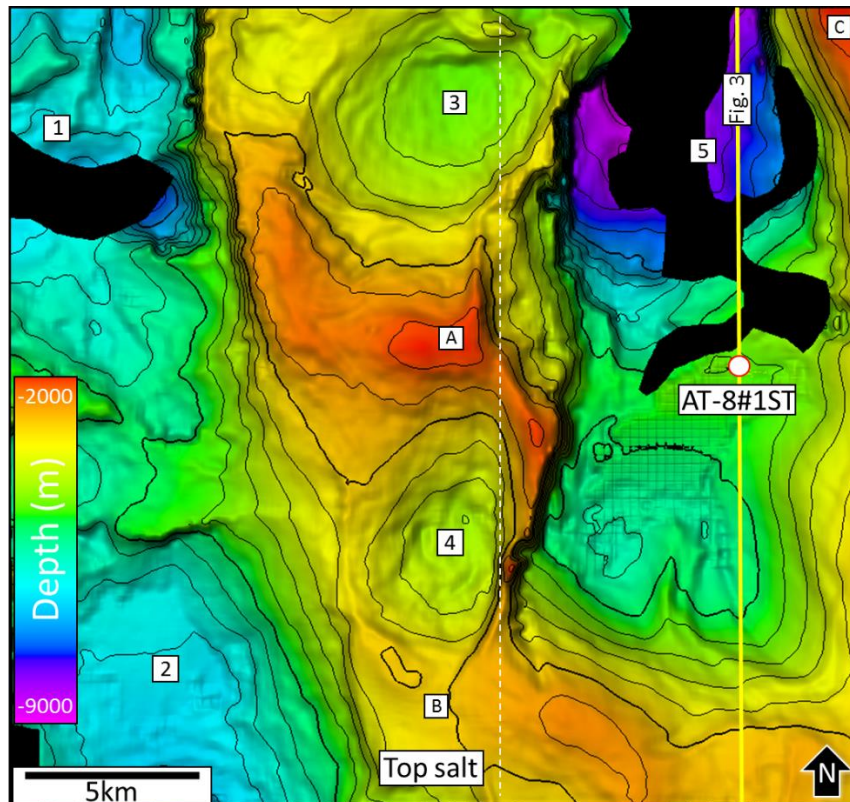


Figure 3A

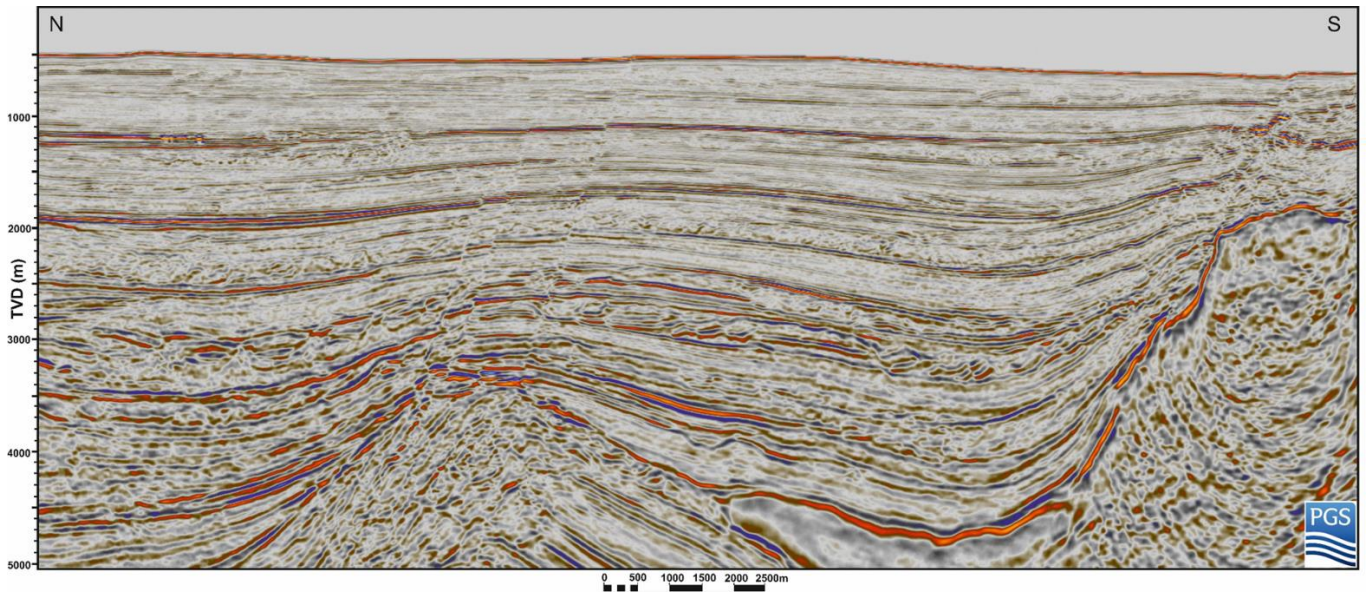


Figure 3B

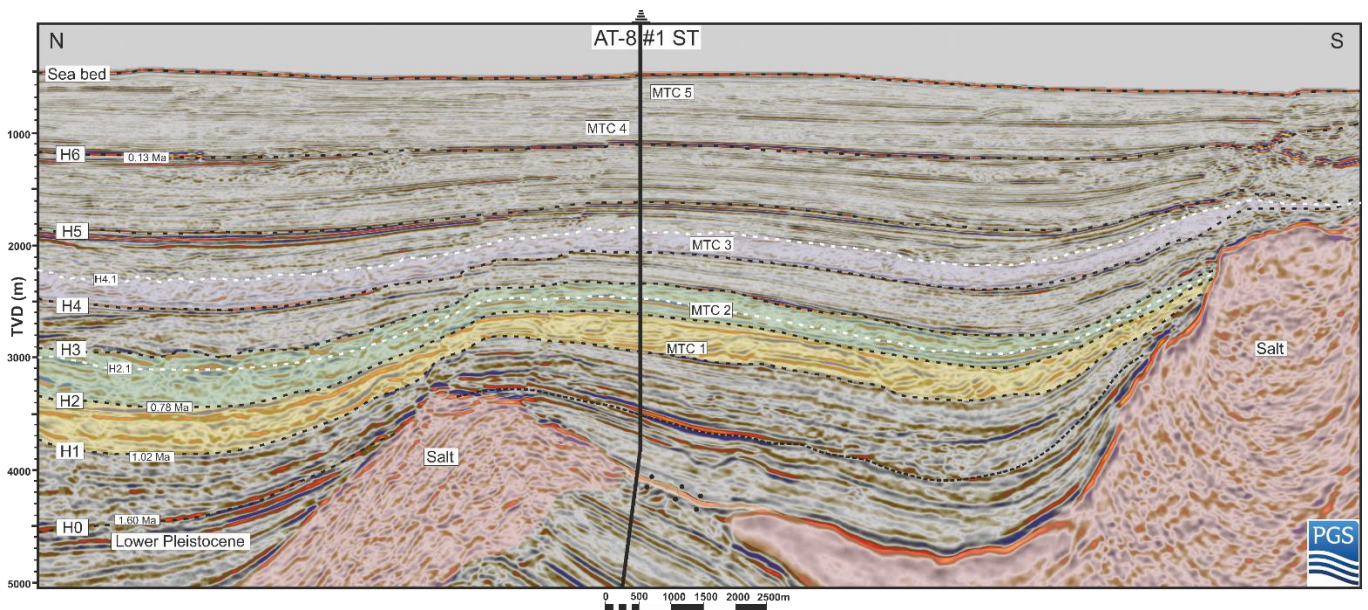


Figure 3C

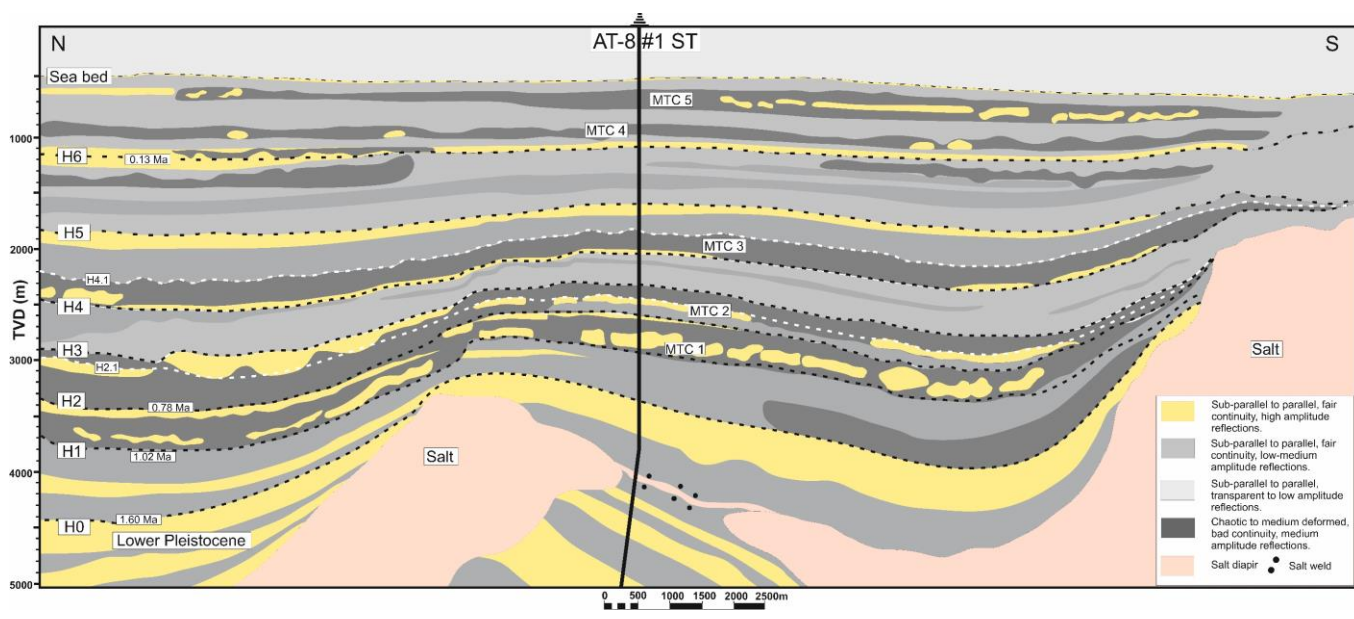


Figure 4A

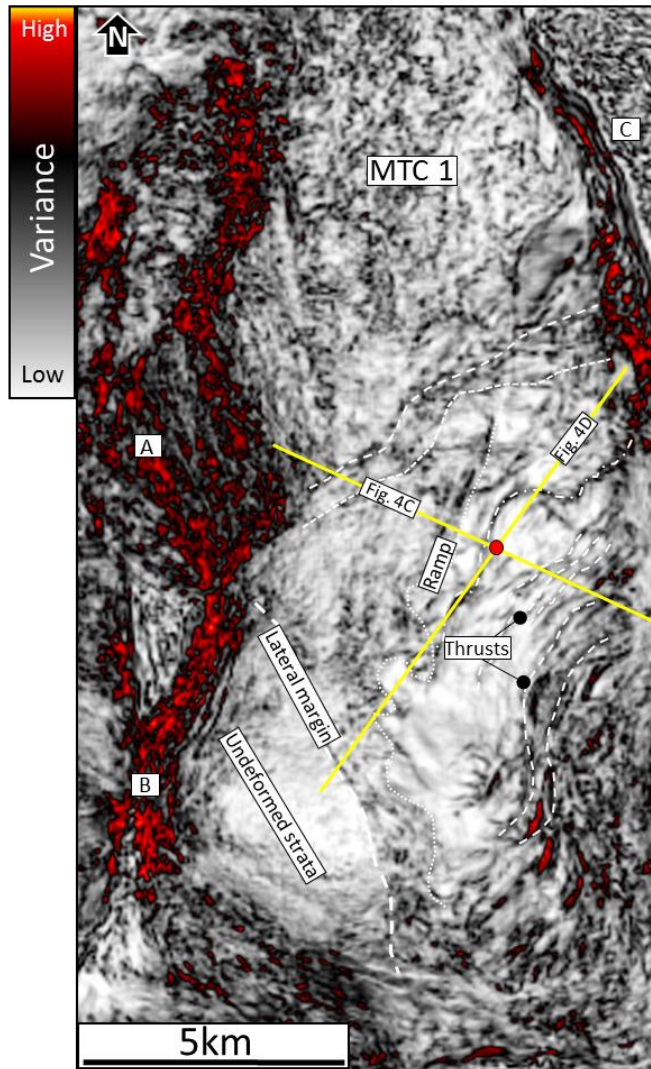


Figure 4B

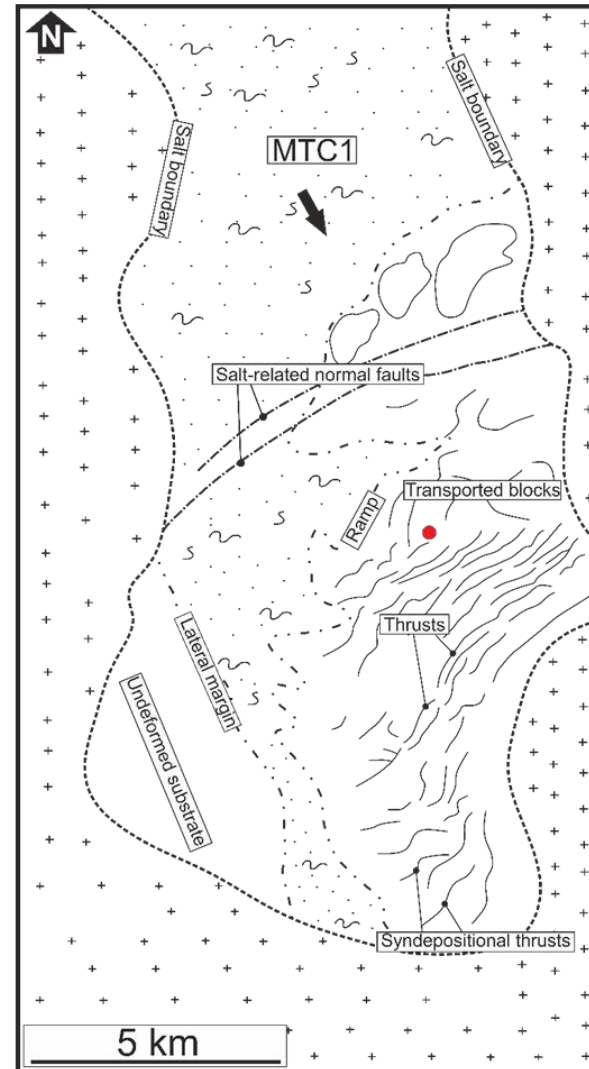


Figure 4C

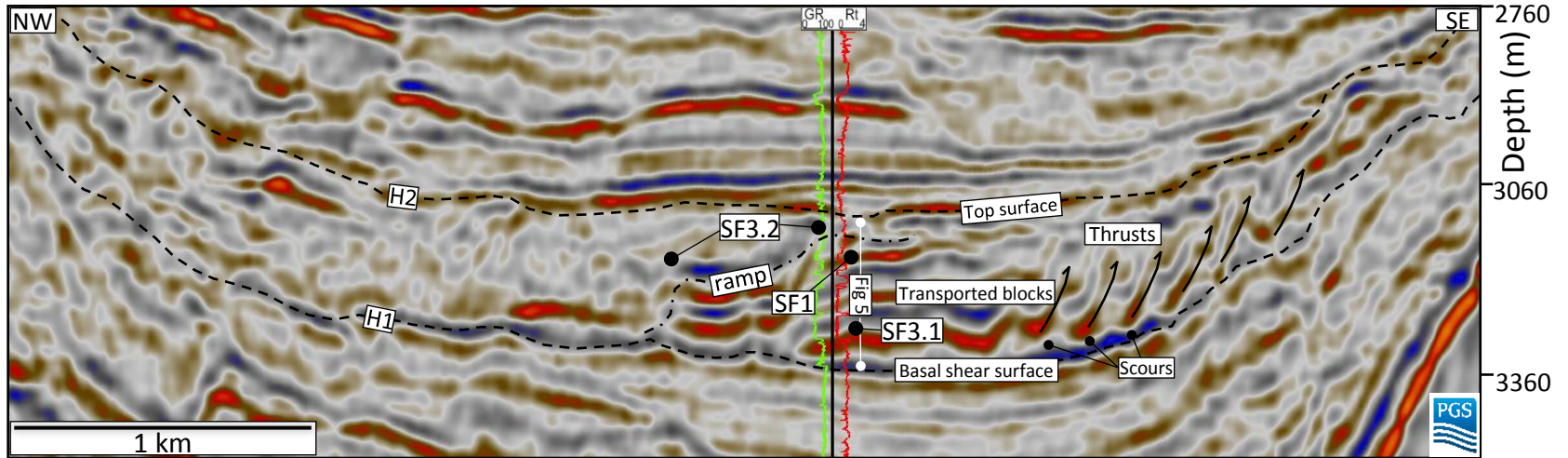


Figure 4D

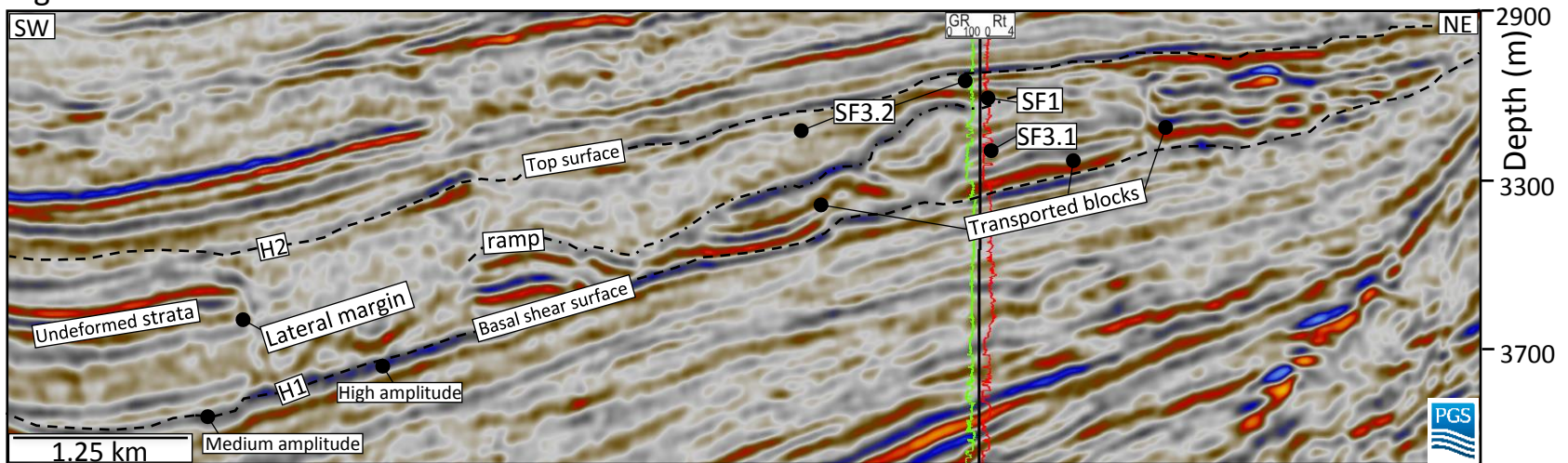


Figure 5A

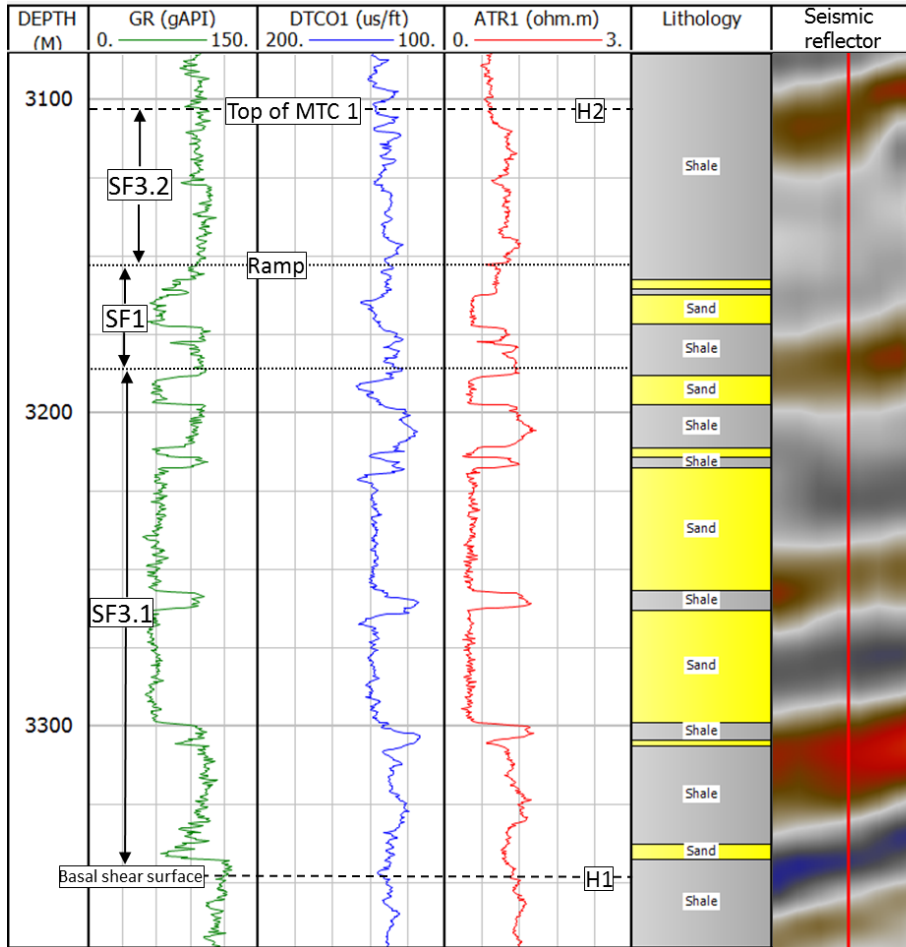


Figure 5B

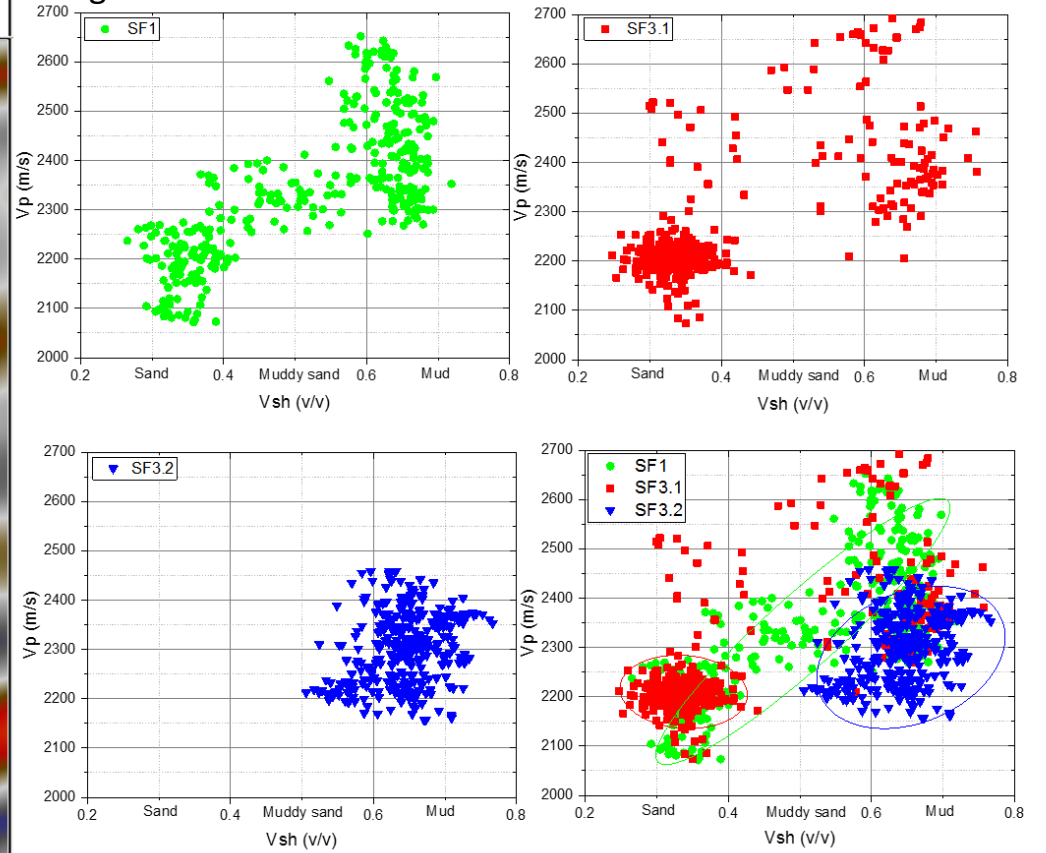


Figure 6A

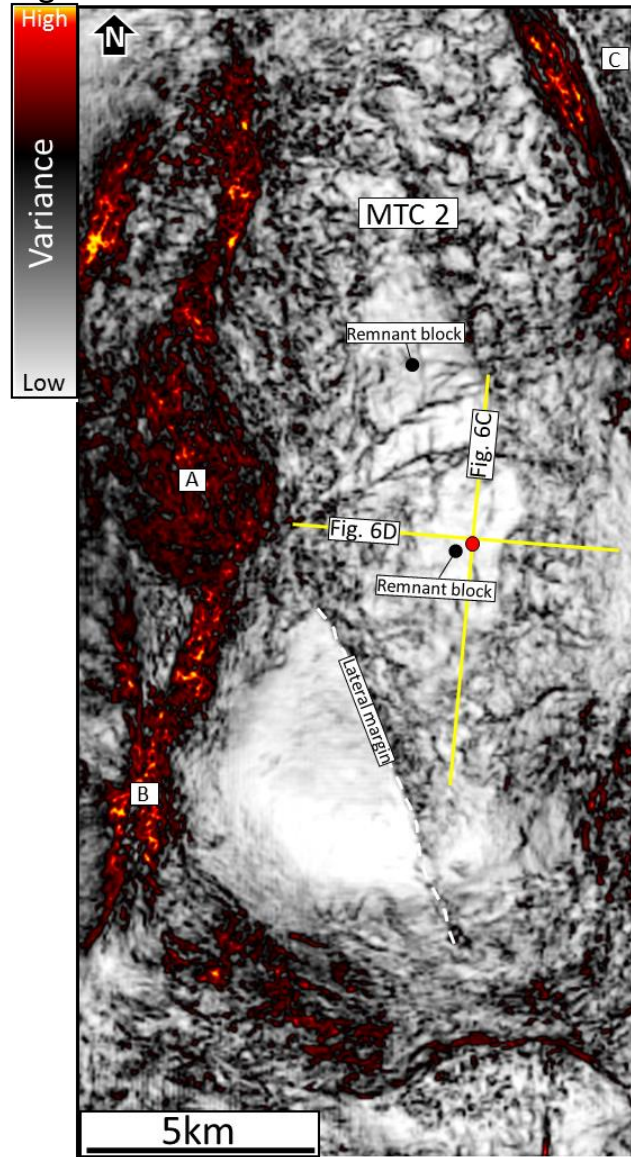


Figure 6B

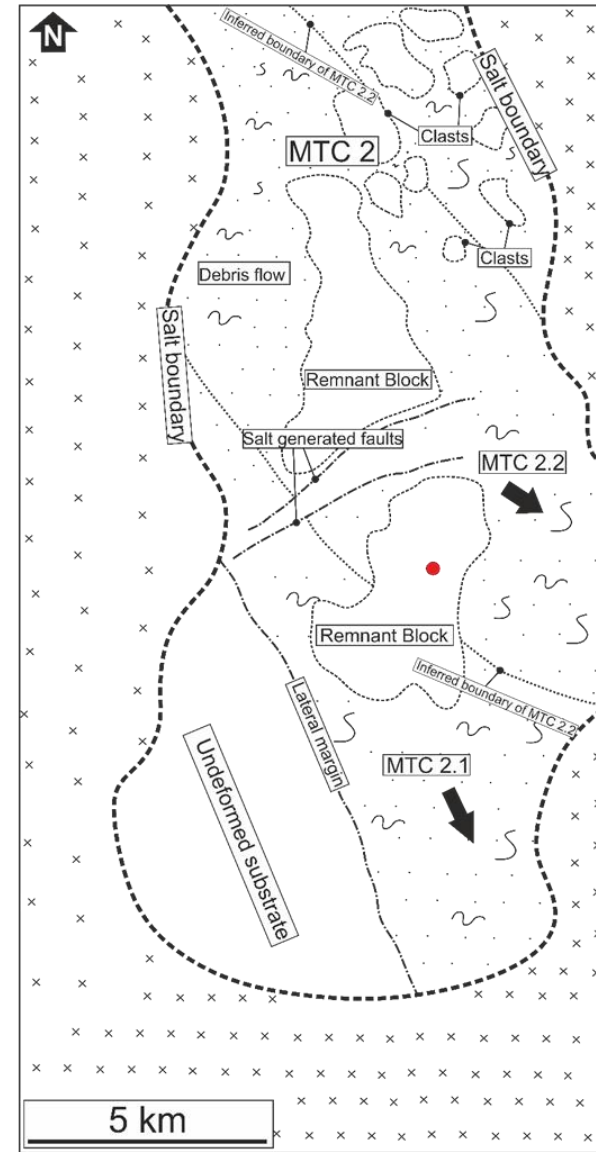


Figure 6C

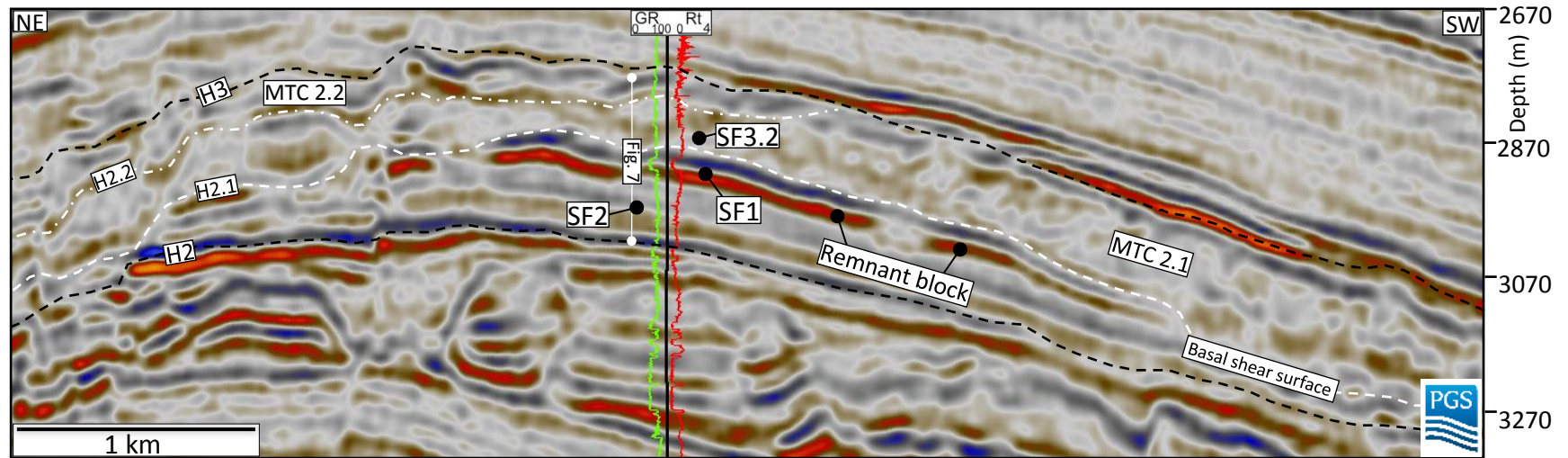


Figure 6D

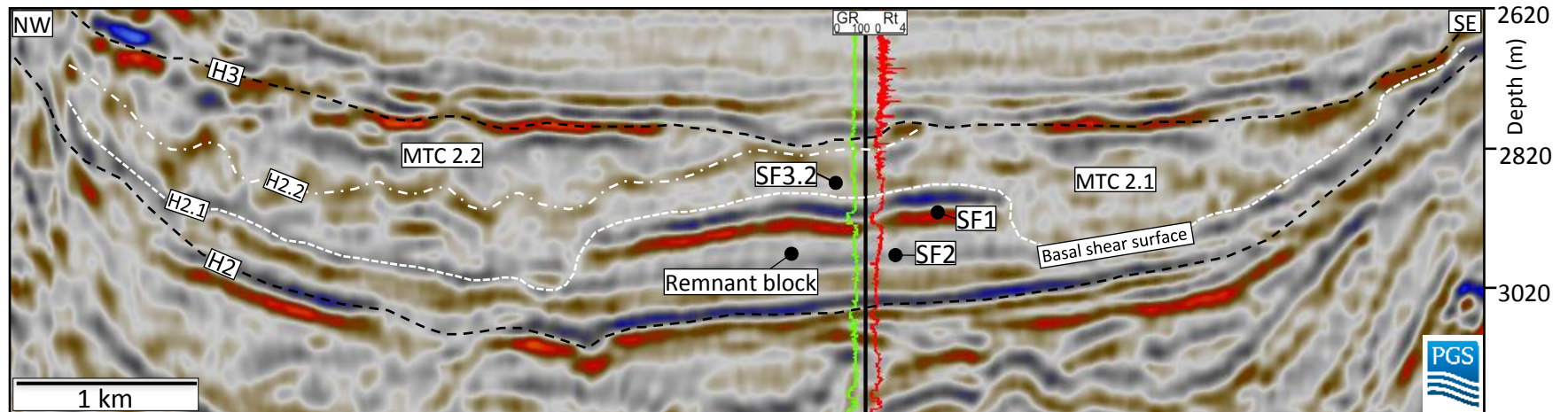


Figure 7A

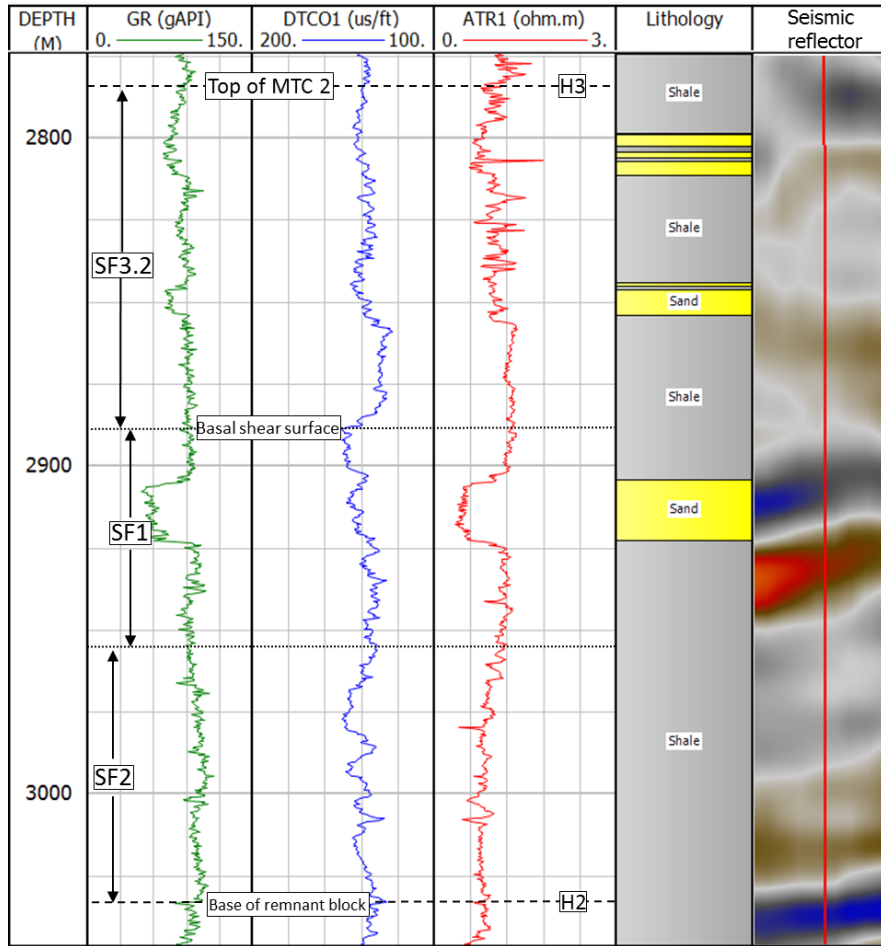


Figure 7B

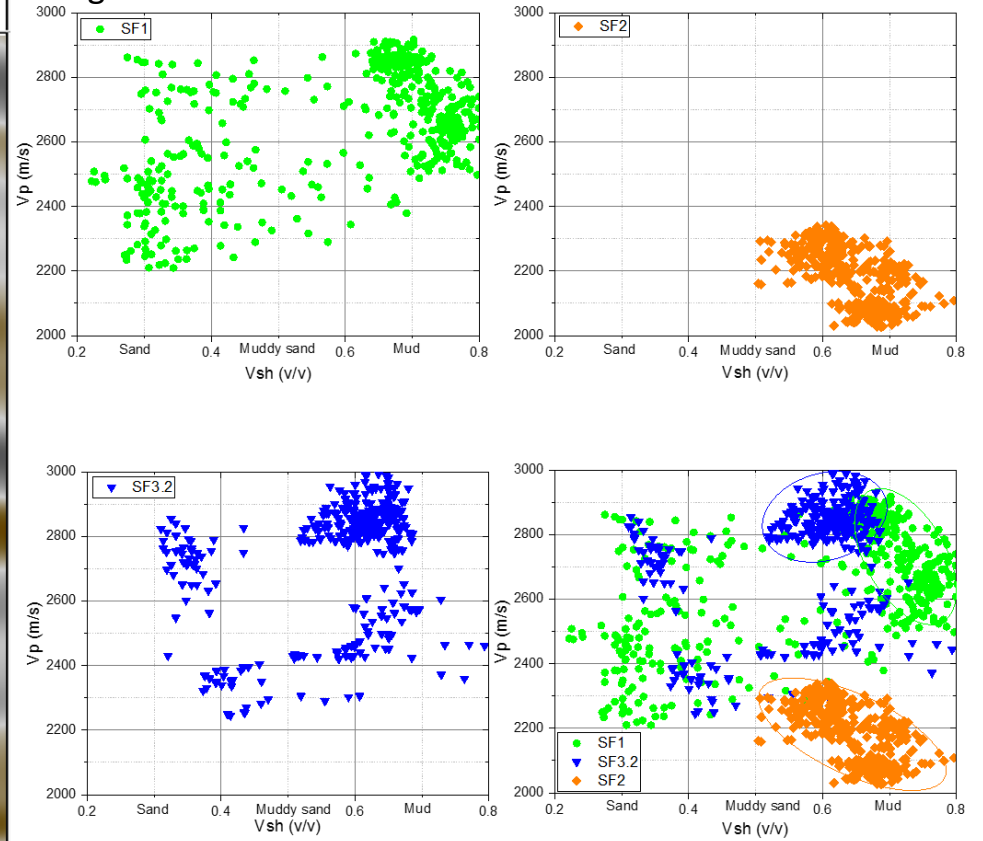


Figure 8A

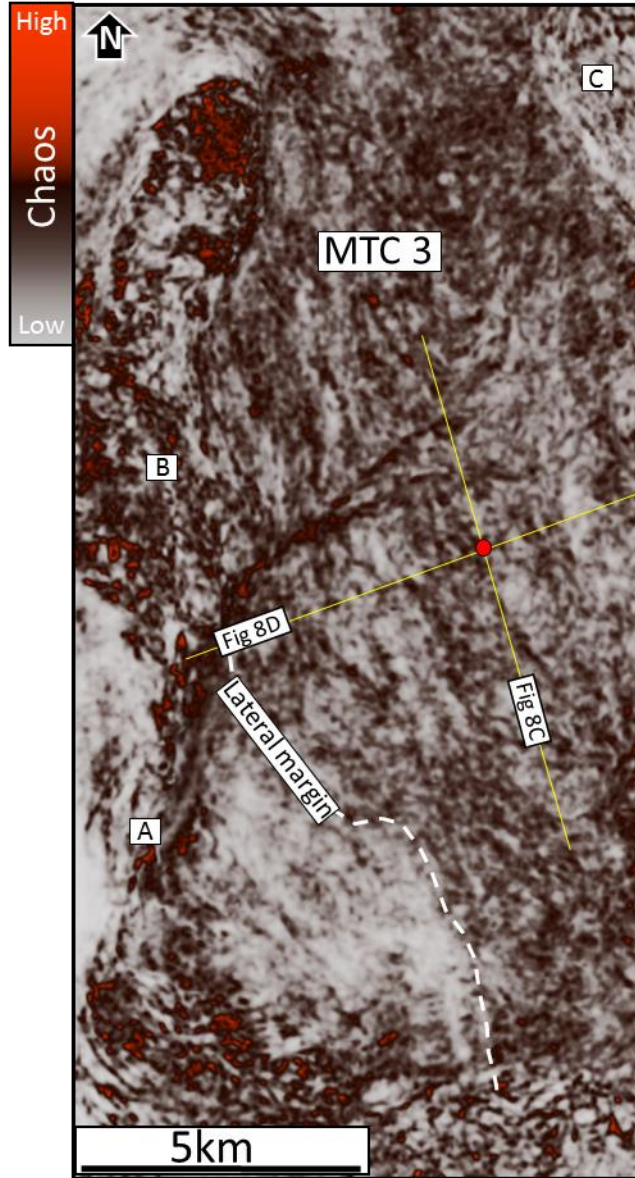


Figure 8B

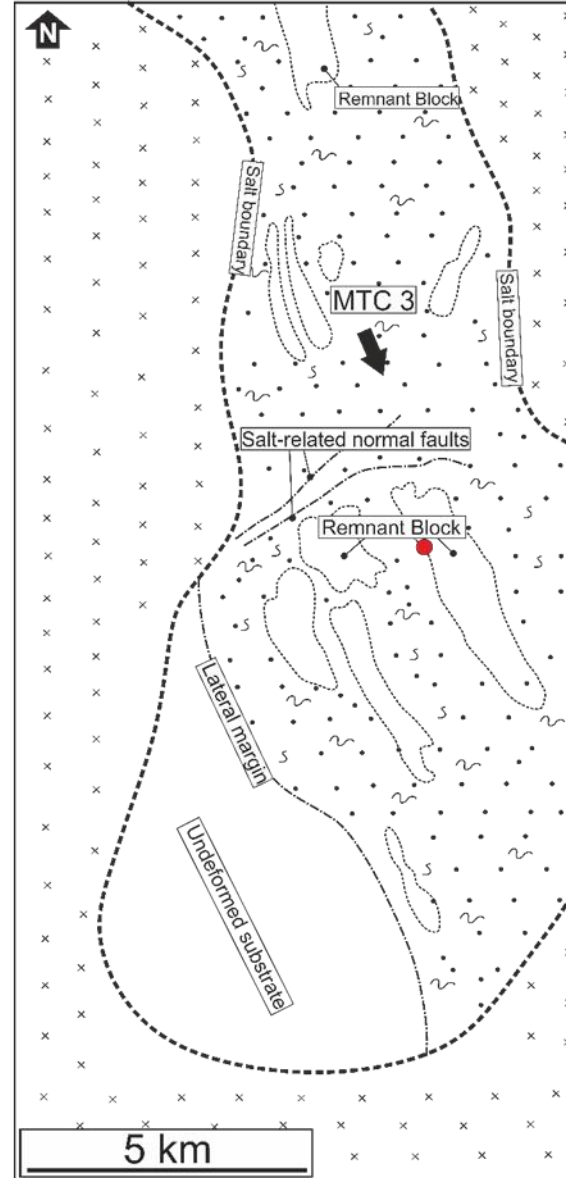


Figure 8C

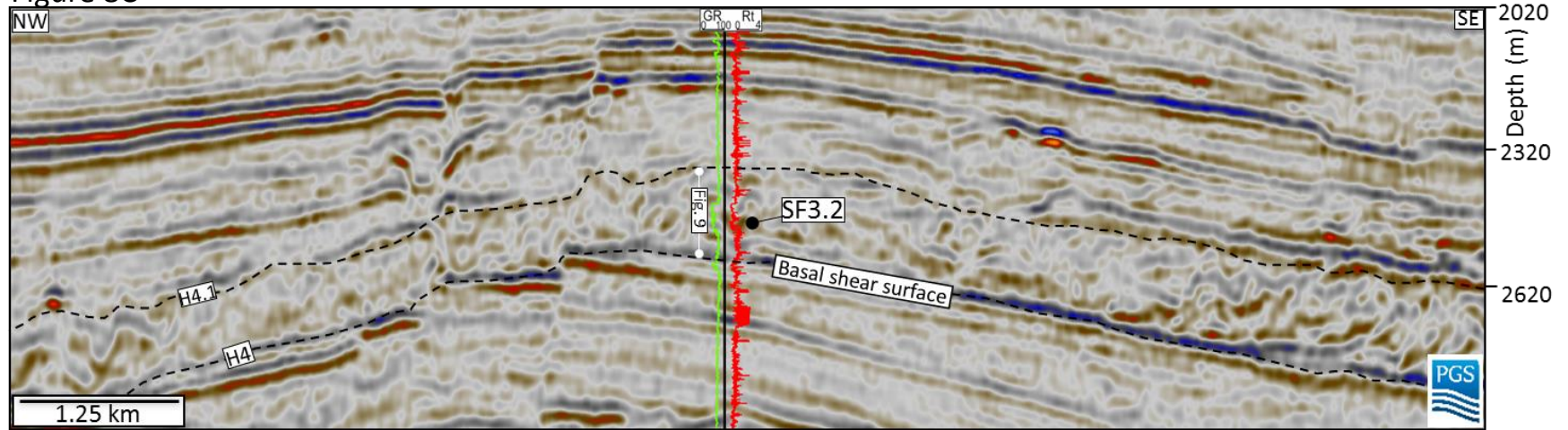


Figure 8D

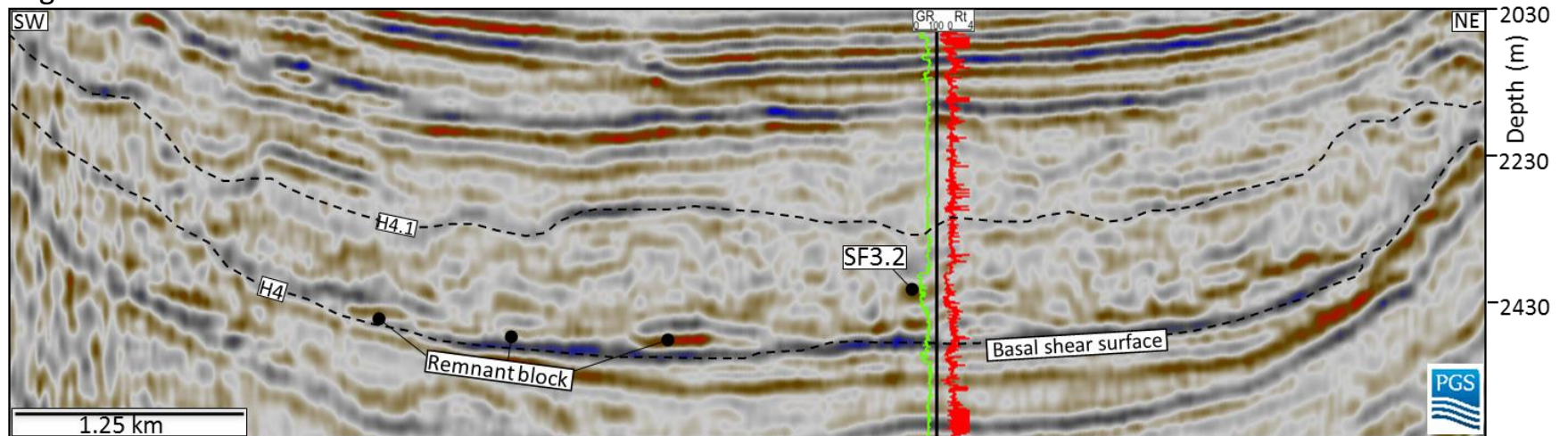


Figure 9A

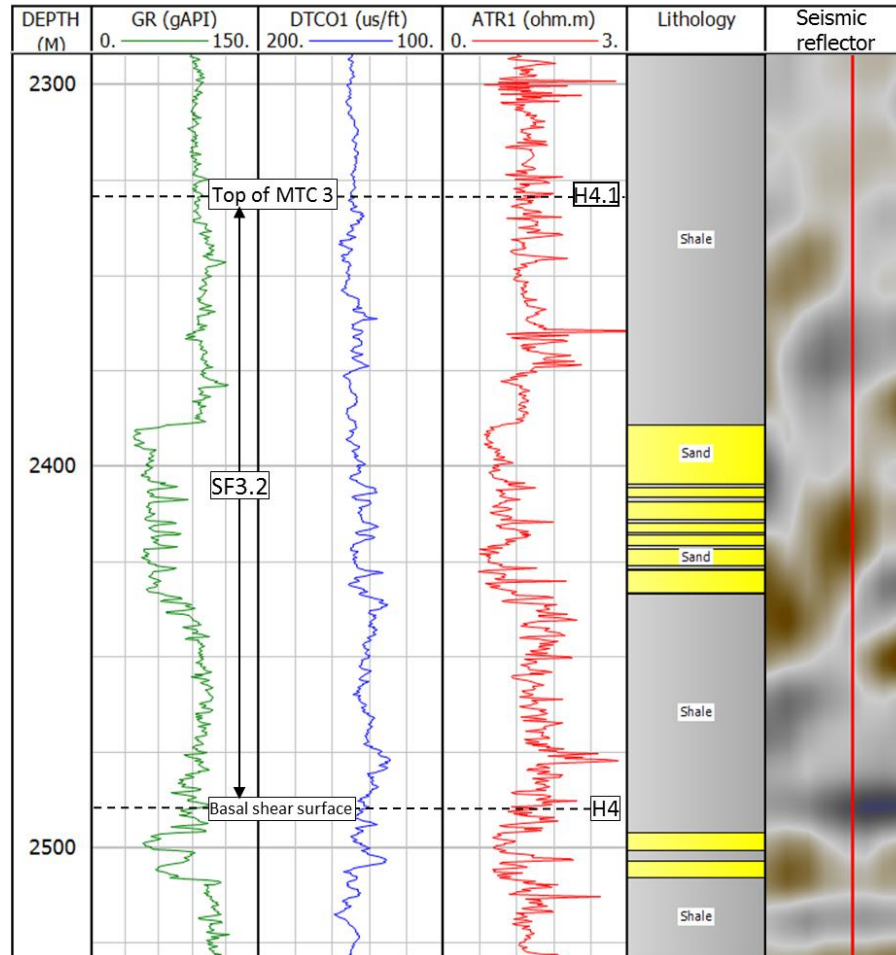


Figure 9B

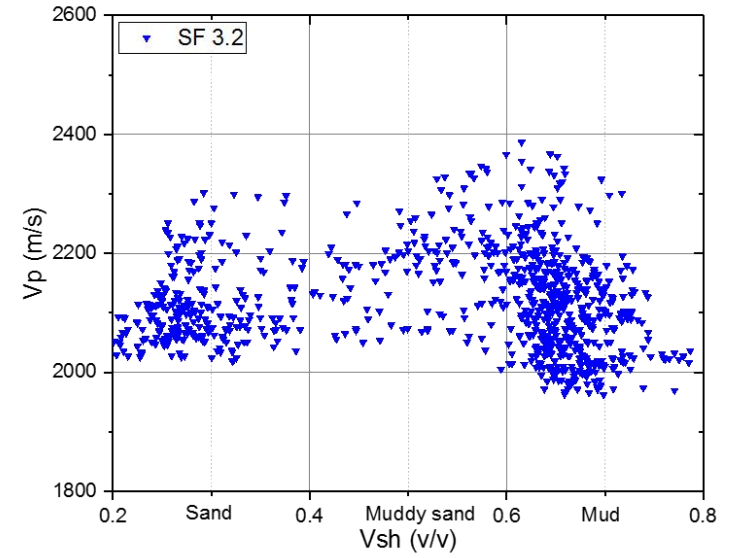


Figure 10A

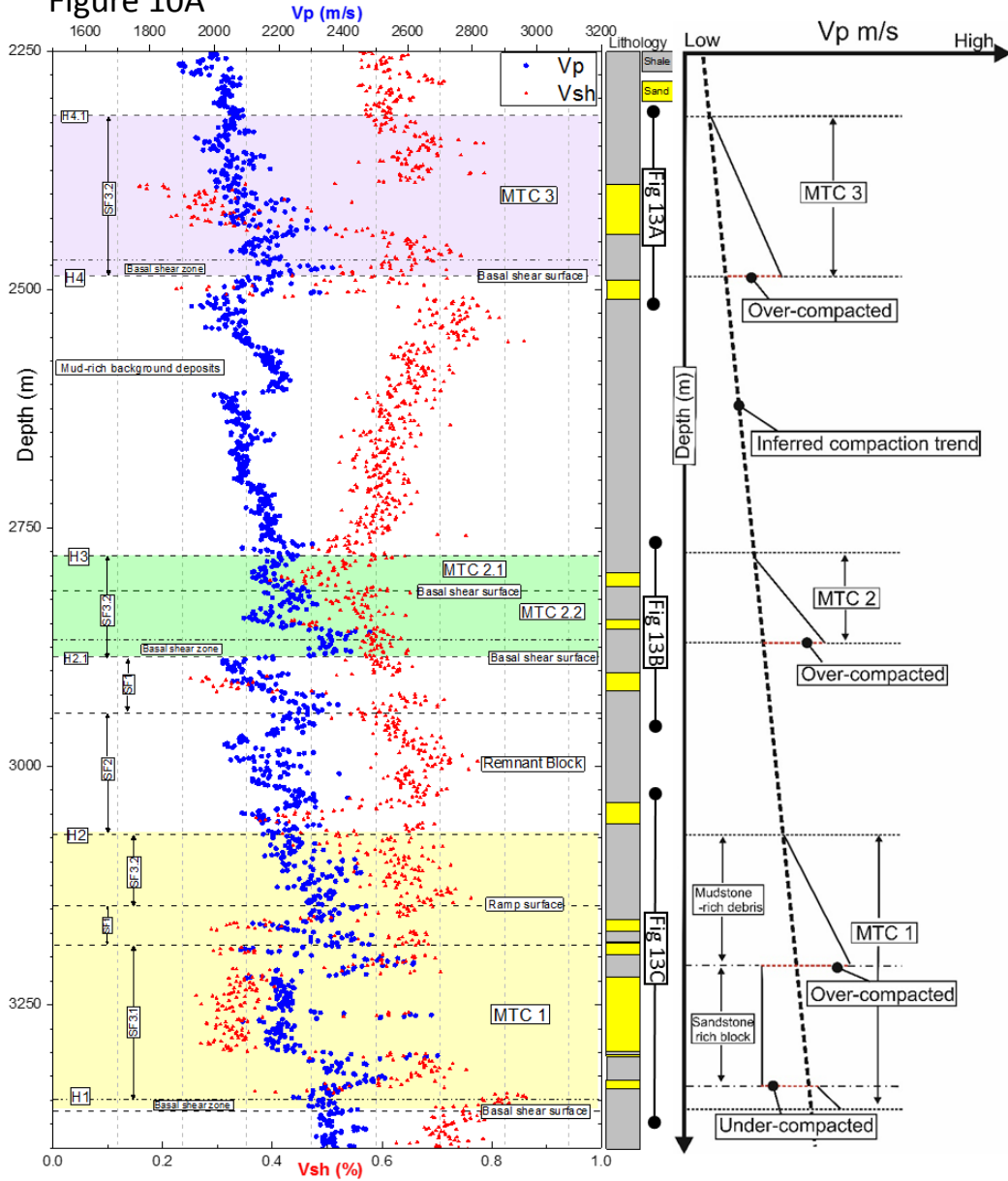


Figure 10B

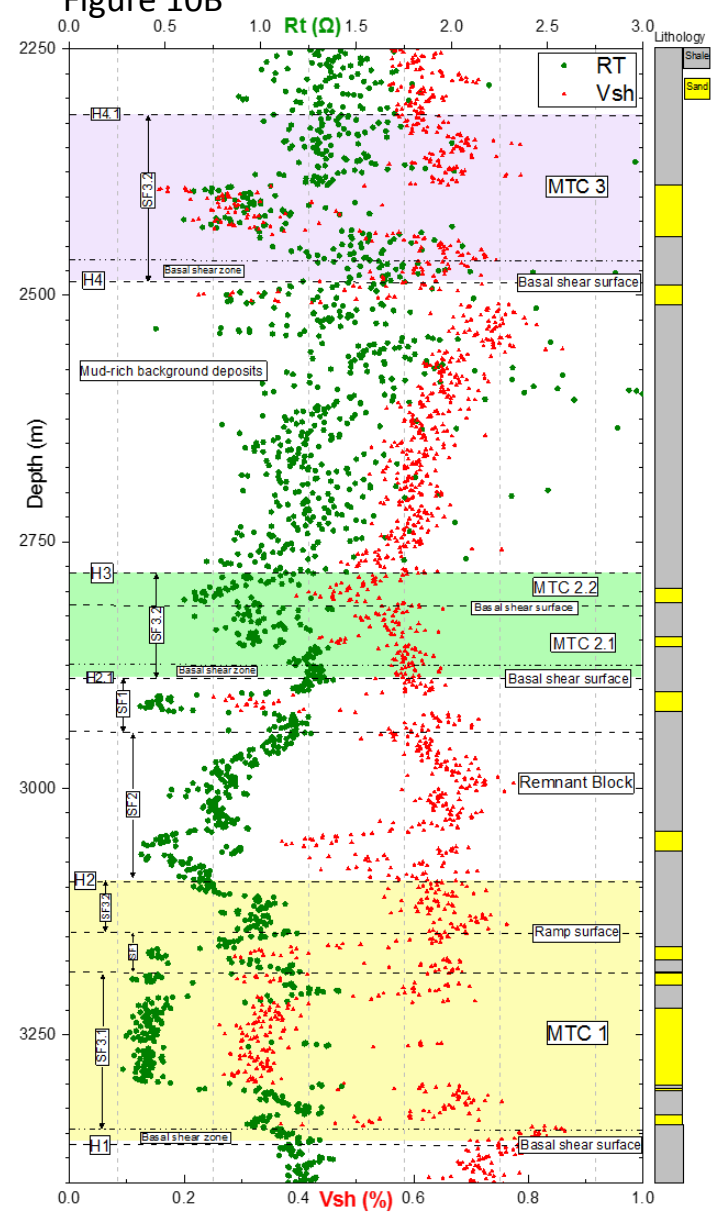


Figure 11A

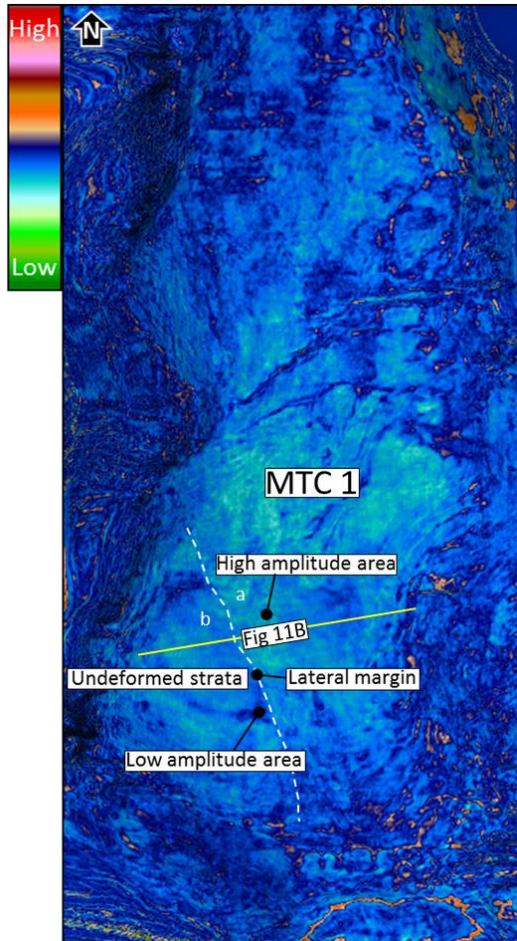
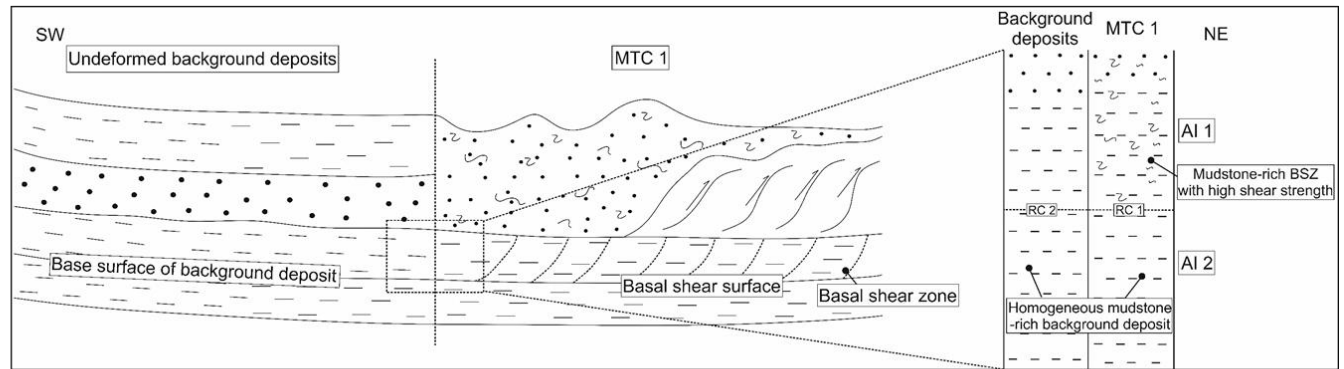


Figure 11B



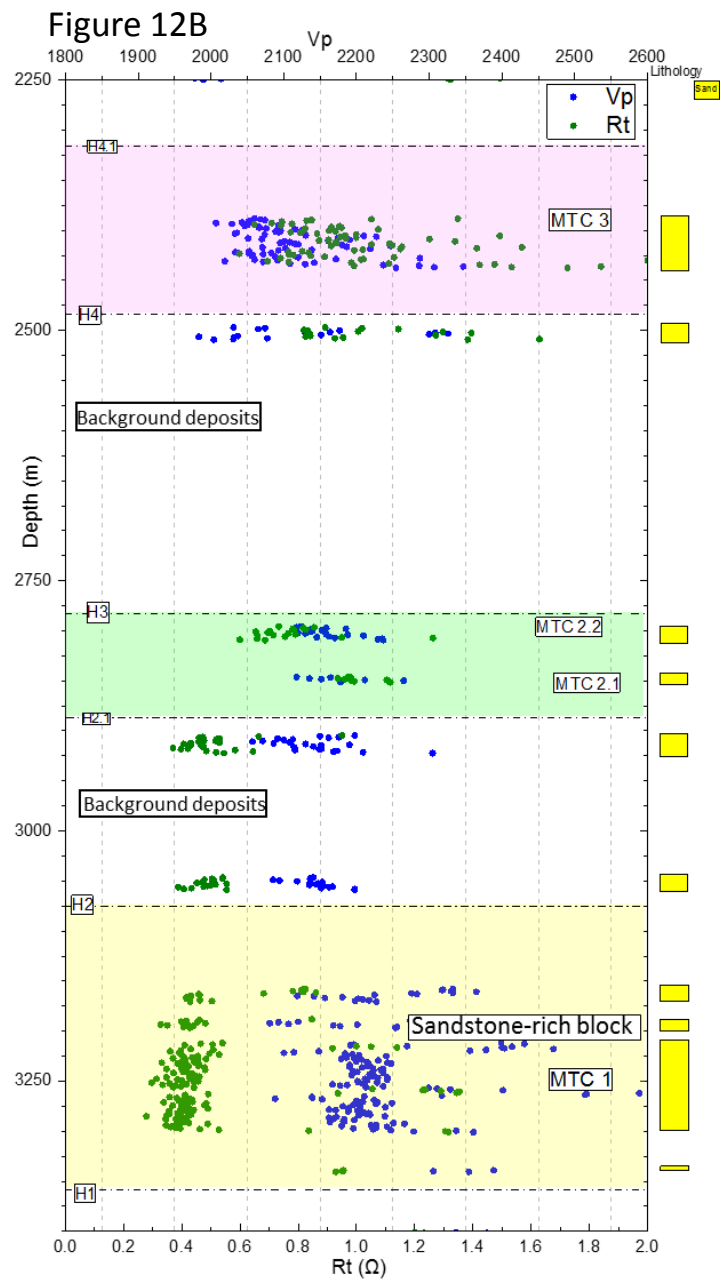
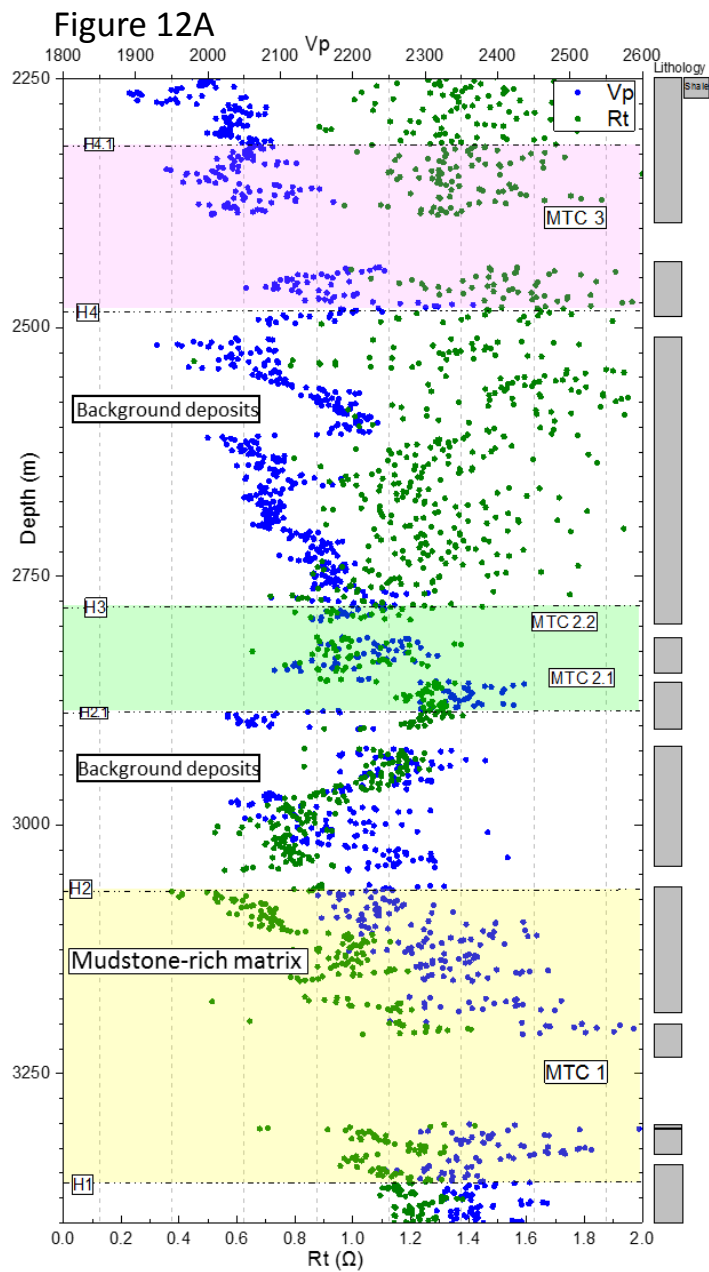


Figure 13A

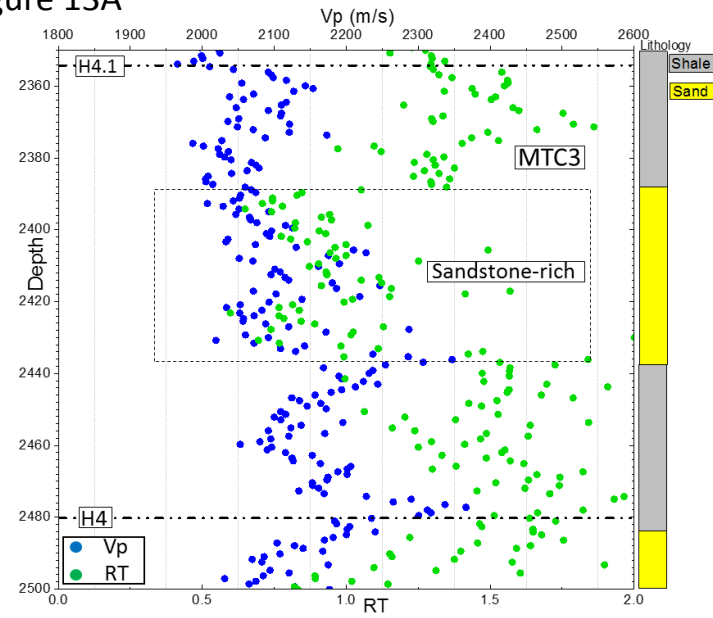


Figure 13B

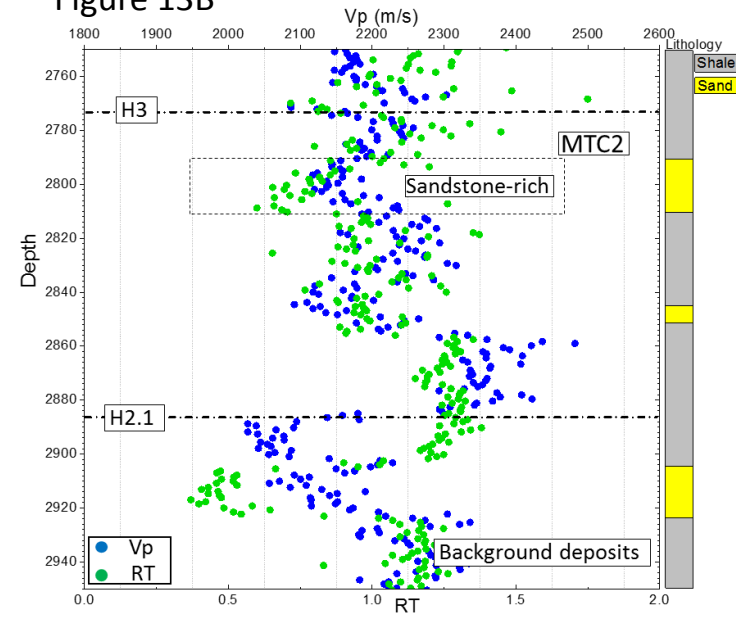


Figure 13C

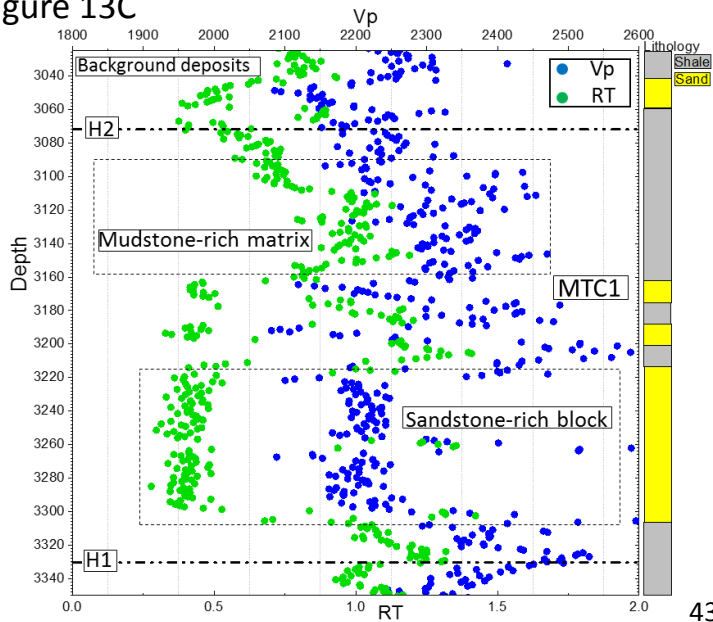


Figure 14

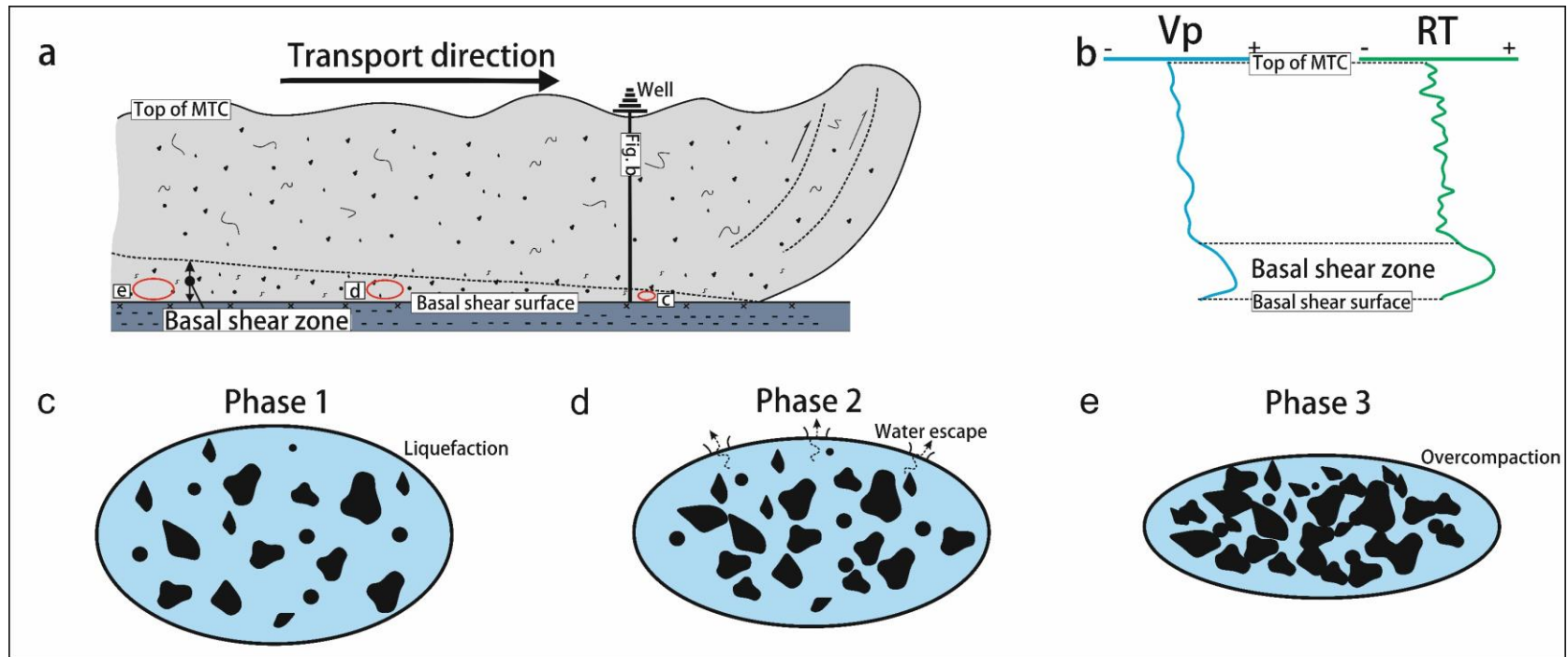


Table 1

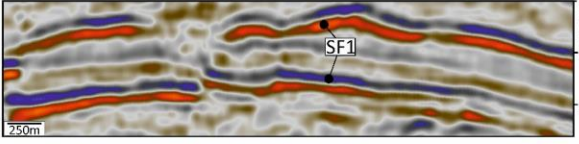


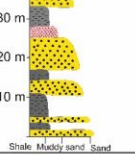
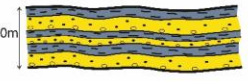
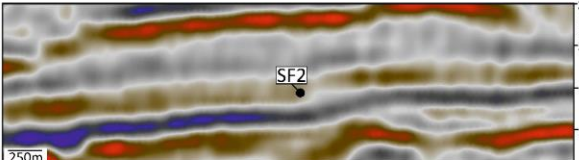


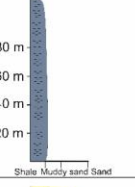
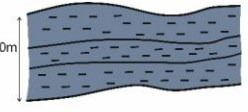
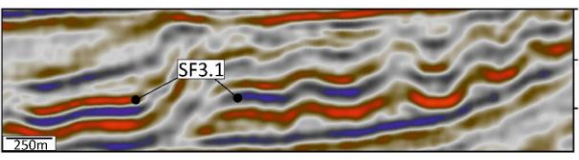


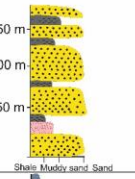

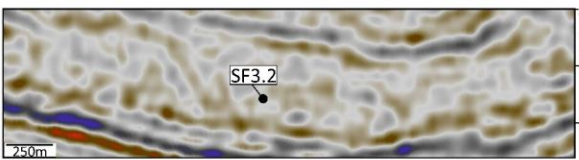


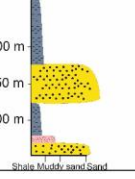
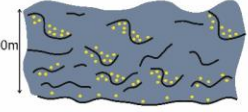
Seismic facies summary							
Types	Seismic sections	GR	Sonic	Lithology	Schematic facies geometries	Facies characteristics	Depositional Enviroment
SF1						Sub-parallel to parallel, fair continuity, high amplitude reflections; seismic reflectors thinning and pitching out to the end. A fining up-ward trend with block low GR response at base and serrated high GR response at top.	Thinly bedded sandstone-rich and mudstone-rich deposits.
SF2						Sub-parallel to parallel reflections, good continuity, with medium to low amplitude reflections; Constantly serrated high GR response.	Background low energy mudstone-rich deposits.
SF3.1						Less deformed, but more continuous, medium to high amplitude reflections; A fining upward trend GR response at base, a set of blocky low GR response at middle, and a fining upward GR response again at top.	Remobilised and transported sandstone-rich blocks
SF3.2						Chaotic reflections, bad continuity with medium to low amplitude reflections; Constantly serrated high GR response or high GR response interbedded with a set of blocky low GR response.	Mixed highly deformed slump deposits with large sandstone-rich blocks.

Table 2

MTC	Thickness (m)	Lithology	Thickness of sandstone rich parts (m)
MTC 1	270 m	Large sandstone-rich blocks with mudstone-rich debris	Approx. 180 m
MTC 2.1	77 m	Mudstone-rich debrite with sandstone-rich blocks	Approx. 30 m
MTC 2.2	43 m	Mudstone-rich debrite	Approx. 10 m
MTC 3	182 m	Mudstone-rich debrite with sandstone-rich blocks	Approx. 70 m